Atmos. Meas. Tech. Discuss., https://doi.org/10.5194/amt-2017-265
Manuscript under review for journal Atmos. Meas. Tech.
Discussion started: 8 September 2017


Atmospheric Measurement Techniques Discussions
Open Access

# High resolution humidity profiles retrieved from wind profiler radar measurements

Frédérique Saïd[1], Bernard Campistron[1], and Paolo Di Girolamo[2]

[1]Laboratoire d'Aérologie, Université de Toulouse, UMR CNRS 5560, Toulouse, France
[1]Scuola di Ingegneria, Universita degli Studi della Basilicata, Potenza, Italy

*Correspondence to:* F. Saïd et al. (frederique.said@aero.obs-mip.fr)

**Abstract.**

Vertical profiles of the atmospheric water vapor mixing ratio are retrieved with an algorithm based on the combination of measurements from an Ultra High Frequency-band wind profiler and radiosoundings at a coarser time resolution. The major advance with respect to previous works is the use of the radar capacity to detect transition levels, such as the top level of the boundary layer, marked by a maximum in the radar reflectivity. This forces the water vapor mixing ratio profile from the free troposphere and from the boundary layer to coincide at this level, after an optimization of the calibration coefficients. The capability of the algorithm to retrieve the humidity vertical profiles for an operational purpose is explored and the results are compared with observations from a Raman lidar.

## 1 Introduction

Over the last 30 years, several authors (Gossard et al., 1982, 1998; Tsuda et al., 2001; Bianco et al., 2005; Stankov et al., 1996, 2003; Furumoto et al., 2003, 2007; Klaus et al., 2006; Imura et al., 2007) discussed the possibility of determining the magnitude of the humidity gradient profiles from measurements of zeroth, first and second moments of wind profiler radars (WPR) Doppler spectra either in the Ultra High Frequency (UHF) or the Very High Frequency range (VHF). The method exploits the clear air scattering properties of electromagnetic waves, this depending on the refractive index and consequently on the pressure, temperature and humidity characteristics of the air. In addition, most of these authors demonstrated the possibility to retrieve humidity profiles, by combining radar measurements with simultaneous measurements from other sensors, i.e. in situ radiosonde observations at a poorer time resolution (Tsuda et al., 2001; Stankov et al., 2003; Furumoto et al., 2006) or remote measurements such as temperature profiles from a radio acoustic sounding system (RASS) (Tsuda et al., 2001), observations from a microwave radiometer profiler (Stankov et al., 1996; Gossard et al., 1998; Bianco et al., 2005; Klaus et al., 2006), precipitable water vapor from a global positioning system (GPS) receiver (Gossard et al., 1999; Imura et al., 2007), or a combination of these measurements. The method was said to be promising for an operational implementation, providing the benefit of a finer time resolution, compared to the conventional radiosonde observations.

However, as far as we know, no successful attempt to apply this method to operational observations has been reported in literature. The first hurdle is related to the missing self-consistency of the method and the required synergy between various

Atmospheric Measurement Techniques Discussions

instruments. Another difficulty is represented by the necessity to carry out accurate measurements of the first three radar Doppler spectra moments, with an accurate calibration of the radar-backscattered power (zeroth order moment) and a careful post-processing of the radar observations. The latter is needed to guarantee that the velocity and width of the spectral peak (first and second order moment respectively) are not disturbed by external contamination such as ground clutter, radio frequency interference, spurious echoes like birds, etc. In addition, the relationship between the refractive index and the radar reflectivity is valid only in clear air conditions and this may raise difficulties when rainfall is mixed with clear air. [1] Radars emitting around 1.3-GHz (UHF) are more sensitive to rainfall than these emitting around 440-MHz (UHF) or 45-MHz (VHF) and require a careful processing to separate multiple-peaks signals in the vicinity of rainfall events. The final hurdle is the fact that the steps to determine the humidity profile from the humidity vertical gradient measured by the WPR is not straightforward and is typically a source of accumulated errors.

In this study, we use WPR observations at 1274-MHz (UHF) collected under a variety of atmospheric conditions at mid-latitudes, and discuss how we cope with the above mentioned difficulties. UHF measurements are combined with successive radiosonde observations, spaced 6 h or longer, to retrieve high-resolution atmospheric humidity profiles. Section 2 provides the theoretical background of the algorithm used to retrieve the humidity profiles. It is based on the method developed by Tsuda et al. (2001). In our modified approach, we introduce a new constraint to integrate the humidity gradient vertical profile, which is the level of transition defined by a reflectivity maximum. This level corresponds either to the top of the mixed or residual layer, or to a temperature and/or humidity discontinuity. This approach modification revealed to be crucial to improve the quality of the results. Section 3 illustrates the experimental sites, the encountered meteorological conditions, the instruments involved in the study and the data processing applied on the WPR measurements. Section 4 illustrates the results of our algorithm under three categories of atmospheric conditions (encountered in the three different datasets) and discusses the calibration coefficients used for each dataset, in relationship with the coefficient values found in the literature. Finally, in section 5, we apply our method to the retrieving of high-resolution humidity profiles between 2 consecutive radiosonde observations and discuss the possibility to use it as an operational product. For one specific dataset we took advantage of the measurements of a ground-based Raman lidar located close to the WPR, to validate the high-frequency (15 min) humidity profiles retrieved by our algorithm.

## 2 Theoretical background

The refractive index of the air $n$, or refractivity $N = (n-1)10^6$, depend on atmospheric thermodynamic properties (Gossard and Sengupta, 1988):

$$N = 77.6\frac{P}{T} + 3.73\,10^5\frac{e}{T^2} \qquad (1)$$

[1] We consider as rainfall the droplets whose size is large enough to be detected by WPRs (typically larger than 10 $\mu$m). By contrast, smaller and saturated particles are considered as cloud particles. In the environment of HyMeX SOP1, the saturated particles easily grow in the presence of marine aerosols and are prone to favor rainfall.

where $T$ is temperature ($K$), $P$ is atmospheric pressure (hPa) and $e$ is water vapor partial pressure (hPa). We can also express $N$ in terms of water vapor mixing ratio (WVMR), $q$ (kg of water vapor per kg of dry air). $q$ is the parameter we aim at retrieving in the present work. Using the approximation $q = 0.622\frac{e}{P-e} \simeq 0.622\frac{e}{P}$, Eq. (1) becomes:

$$N = 77.6\,\frac{P}{T} + 5.99\,10^5\,\frac{Pq}{T^2} \tag{2}$$

The vertical gradient of refractivity $M$ (m$^{-1}$) can be calculated by applying the following linearized equation for small perturbations (Gossard and Sengupta, 1988):

$$M = \frac{\partial N}{\partial T}\frac{dT}{dz} + \frac{\partial N}{\partial q}\frac{dq}{dz} \tag{3}$$

where

$$\frac{\partial N}{\partial T} = -77.6\,\frac{P}{T^2} - 1.2\,10^6\,\frac{Pq}{T^3} \tag{4}$$

$$\frac{\partial N}{\partial q} = 5.99.\,10^5\,\frac{P}{T^2} \tag{5}$$

Equation (3) leads to:

$$M = \frac{dN}{dz} = -77.6\frac{P}{T^2}\frac{dT}{dz} - 1,2\,10^6\frac{Pq}{T^3}\frac{dT}{dz} + 5.99\,10^5\frac{P}{T^2}\frac{dq}{dz} \tag{6}$$

which shows that the refractivity vertical gradient consists of 3 different terms: the temperature gradient term (term 1), the WVMR at level $z$ term (term 2), the humidity gradient term (term 3). As underlined by Tsuda et al. (2001), term 1 may be dominant under dry conditions such as winter conditions at mid-latitudes or in the upper atmosphere. They also found that term 2 usually contributes less than 10 %, even close to the surface where $q$ is the larger. The dominant contribution of term 3, depending on $\frac{dq}{dz}$ allows to solve very easily the first-order differential Eq. (6) (Tsuda et al., 2001). Some authors (Gossard et al., 1998; Stankov et al., 2003) consider that the partial derivatives in Eq. (5) are constant and can be estimated from standard atmosphere profiles. This assumption also imposes to neglect the contribution by the second term. In this paper we do not make this assumption, especially because one of our datasets is characterized by relatively moist conditions near the surface, which imposes to consider the 3 terms in Eq. (6). As also demonstrated by Tsuda et al. (2001), the differential Eq. (6) can be solved after introducing the Brunt-Vaïssala frequency $N_{BV}$ (s$^{-1}$) given by:

$$(N_{BV})^2 = \frac{g}{\theta}\frac{d\theta}{dz} = g\frac{dln\theta}{dz} \tag{7}$$

where $\theta = \left(\frac{1000}{P}\right)^{2/7}$ and $g$ are the air potential temperature ($K$) and the acceleration of gravity (m s$^{-2}$), respectively.

This leads to:

$$M = 5.99\,10^5 \frac{P}{T^2}\frac{dq}{dz} - 1.2\,10^6 \frac{Pq}{T^2}\frac{(N_{BV})^2}{g} - 77.6\frac{P}{T}\frac{(N_{BV})^2}{g} \tag{8}$$

which can be written (Tsuda et al., 2001) in the form:

$$\frac{dq}{dz} + A(z)q = B(z) \tag{9}$$

where:

$$A(z) = \quad -2\,\frac{(N_{BV})^2}{g}, \tag{10}$$

$$B(z) = \quad 1.65\,\frac{T^2}{P}M + \frac{1}{7750}\left(\frac{dT}{dz} + \Gamma\right). \tag{11}$$

where $\Gamma$ = 9.8 $10^{-3}$ K m$^{-1}$ is the dry adiabatic temperature lapse rate. Tsuda et al. (2001) provided the following final form for Eq. (9):

$$q(z) = \theta^2 \int_{zo}^{z} (1.67.10^{-6}\frac{MT^2}{P} + \frac{1}{7750}\frac{d\theta}{dz})\theta^{-2}dz + q_o \tag{12}$$

with $q_o$ being the WVMR at level $z_o$ where the integration is initialized.

Following Tsuda et al. (2001), Furumoto et al. (2006), Klaus et al. (2006) and Imura et al. (2007) also used Eq. (12) to compute humidity profiles. We use this equation in the present work.

The next step is to relate $M$ to the radar characteristics. In clear air (precipitation-free atmosphere), UHF-range and VHF-range profilers detect the fluctuations of refractive index with a scale of one-half the radar wavelength, through the following expression Ottersten (1969):

$$\eta = 0.38\,C_n^2\,\lambda^{-1/3} \tag{13}$$

where $\eta$ is the volume reflectivity for the turbulence echo (m$^{-1}$), depending on the radar return signal power, $\lambda$ is the wavelength and $C_n^2$ is the turbulence structure parameter (m$^{-2/3}$) for the radar refractive index. Gossard et al. (1982, 1998) found that, for homogeneous isotropic turbulence in a horizontally homogeneous medium with vertical gradients of mean properties, the squared vertical gradient of potential refractivity (potential refractivity is the value of $N$ for an air parcel moving adiabatically from its ambient level to the reference level -1000 hPa- without loss or gain of moisture) is:

$$\left(\frac{d\Phi}{dz}\right)^2 = \left(\frac{L_w}{L_\phi}\right)^{\frac{4}{3}} \left(\frac{dV}{dz}\right)^2 \frac{C_n^2}{C_w^2} \tag{14}$$

According to Tatarskii (1971) , $\frac{L_w}{L_\phi}$ is the ratio of two outer lengthscales, for shear and for potential refractive index, respectively. Gossard et al. (1982) provided an empirical formulation for this ratio which they refined in Gossard et al. (1998). They found this ratio to be very small in stable layers and large in zones with near-neutral stability, with values ranging between 2 and 6. In this expression $\frac{dV}{dz}$ is the vertical shear of the horizontal wind $V$, $C_w^2$ is the structure parameter of vertical velocity which can be expressed in term of the dissipation rate of the turbulent kinetic energy $\epsilon$ (m$^2$ s$^{-3}$) through the expression: $C_w^2 = \frac{4}{3}\, 2.1\, \epsilon^{\frac{2}{3}}$ (where 2.1 is the Kolmogorov constant).
Assuming that $M^2 = \left(\frac{d\Phi}{dz}\right)^2$, Eq. (14) gets the form:

$$C_n^2 = \alpha^2 \, \frac{\epsilon^{2/3}\, M^2}{\left(\frac{dV}{dz}\right)^2} \tag{15}$$

Here, the first three moments of the radar spectral data are involved. Specifically, $C_n^2$ is related to the zeroth moment since the volume reflectivity $\eta$ in Eq. (13) is proportional to the backscattering signal power. The proportion coefficient $K$ between $\eta$ and the backscattering signal power depends on the radar properties including antenna efficiency, receiver bandwith, system noise power, losses in the transmission lines, etc. In most studies, $K$ is not known since the radar is not calibrated, so $K$ is included in the term $\alpha^2$ of Eq. (15). The coefficient $\alpha^2$ will be further discussed later.

$V$ is determined from the first moment, the Doppler shift in the spectral data, obtained at the end of the radar computation process. $\epsilon$ is related to the estimation of the second moment, the broadening of the radar spectra.

Let now discuss the coefficient $\alpha^2$. Assuming that the radar is calibrated, so that $K$ is known and the structure coefficient $C_n^2$ is an absolute value, Gossard et al. (1998) took a constant value for $\alpha^2$ of 0.44 regardless of the $M^2$ profile and the considered level in the profile. This value is obtained by comparing refractive index profiles obtained from balloon measurements to those estimated by a 440-MHz UHF radar, after an accurate post-processing of the first and second moments of the spectral data and an accurate radar calibration (that provided $K$). In fact, they measured an average value for $\frac{L_w}{L_\phi}$ of 4, which, after Gossard et al. (1982), should be considered as conservative under steady conditions.

Following Ottersten (1969), Gossard et al. (1982) and Stankov et al. (2003) used another expression for the turbulence structure parameter, based on the energy equation:

$$C_n^2 = a^2 \, \frac{\epsilon^{2/3}\, M^2}{\left(\frac{dV}{dz}\right)^2} \, (1 - R_f)^{-1} \tag{16}$$

where $R_f$ is the flux Richardson number. They indicate that this relation is valid under fairly general assumptions inside regions of large kinetic energy transfer from shear into turbulence. A value of 2.8 is used for $a^2$.

For the specific case of a free troposphere which is most of the time hydrostatically stable and where the turbulence is known to be intermittent (in time and space), VanZandt et al. (1978) refined this relation by inserting $F$, a 'filling factor', which accounts for the turbulent fraction of the backscattering volume.

$$C_n^2 = 2.8\,\frac{\epsilon^{2/3} M^2}{\left(\frac{dV}{dz}\right)^2}(1-R_f)^{-1}F^{1/3} \tag{17}$$

VanZandt et al. (1978) provided an estimation of $F$ based upon a simple model for the statistical distribution of wind shear and potential temperature gradient. The comparison of Eq. (15) and Eq. (17) reveals that $\alpha^2$ should depend on the stability conditions in both the ABL and free troposphere, and also on the 'filling factor' in the free troposphere. In agreement with the concept of 'filling factor', Gossard et al. (1999) noticed that $\alpha^2$ could depend on anisotropy or turbulence unsteadiness. Tsuda et al. (2001) considered that $\alpha^2$ is not constant and requires calibration, even if the radar calibration coefficient $K$ is known. In the present work, we will pay special attention to the coefficient $\alpha^2$.

To summarize, the first three moments of the radar spectrum allow to determine $M^2$ (Eq. (15)), provided that $\alpha^2$ is known. The sign of $M$ remains however ambiguous. In most cases it is negative, but it can become positive under clouds or in locally dry layers. Supposing that the ambiguity is resolved, the computation of $q$ through Eq. (12) requires the knowledge of the initial condition $q_o$ and of the potential temperature and pressure profiles (or at least an estimation of the air density at the surface to derive the pressure from the temperature profile). As underlined by Klaus et al. (2006), the estimation of a single humidity profile requires simultaneous measurements of 4 data-inputs, beside the radar measurements.

As already mentioned in the introduction, several authors proposed to get the temperature profiles from simultaneous RASS observations, and the initial density and humidity conditions by a meteorological station at the surface. This however raises an issue since the first radar gate is not at the surface and since the signal-to-noise is sometimes disturbed at the lower gates.

Other authors used the combination of radar wind profilers and ground-based microwave radiometers, the latter providing both temperature and humidity profiles, but at a coarser vertical resolution than the profiler vertical resolution. The first advantage of this method is represented by the possibility to calibrate the radar estimate of the $\mid M \mid$ value using the radiometer integrated humidity on the air column. A second advantage is represented by the possibility to determine the sign of $M$ from the radiometer humidity profile, as in fact this sign is the same as the sign of the humidity gradient, or negative if the humidity gradient is negligible.

The integrated value of humidity on the air column can also be obtained from the GPS data and is sometimes used as a constraint for the calibration of $\mid M \mid$, provided that at least one in-situ humidity profile is available (e.g. from a radiosonde) to calculate the amount of the integrated humidity in the height range where the profiler identifies echoes relative to the total column integrated humidity. This method also assumes that this contribution is constant, which is a rough hypothesis, difficult to fulfill, especially because of the variability in the radar detection height.

Finally, another method consists in using low time resolution radiosonde profiles (6-hour or 9-hour spaced) to initialize $q$, calibrate $M$ and provide the temperature and pressure profiles. Then the objective with the radar is to provide intermediate profiles with a finer time resolution. This is the method we decided to use in the present work. In addition, we propose two refinements. Usually, the integration shown in Eq. (12) is initialized at the lowest gate measured by the radar, or, if the latter is too high and observation not available, at the upper boundary where $q$ becomes nearly zero (Tsuda et al., 2001). Here, we make two integrations. The first is started near the first radar gate, which is between 150 and 375 m AGL according to the radar and the measurement mode (see next section), while the second is started at the upper boundary of the radar profile, which is never the same since it depends on the backscattered echo power (the detectability is enhanced under moist conditions and reduced under very dry conditions). Both integrated profiles are adjusted (by joining the points) at a characteristic height that we will call Hlim. Hlim may correspond to the top level of the atmospheric boundary layer (ABL), under unstable conditions, or at least to a strong moisture gradient under neutral or stable conditions. This level is easily detected by the WPRs, since it corresponds to a local maximum in the radar reflectivity profile. Hlim has been used for the past 20 years to monitor the depth of the mixed ABL Zi (Angevine et al., 1994; Heo et al., 2003).

Since this level can demarcate two regions of the low troposphere, characterized by (potentially) drastically different turbulent conditions, we decided to compute $\alpha^2$ independently in both part of the profiles: below and above Hlim. $\alpha^2$ was determined in each of these regions by computing $M_{RS}^2 / M_r^2$. $M_{RS}^2$ is calculated from the radiosonde observations through Eq. (6) and $M_r^2$ from the WPR data through Eq. (15). This calibration step could have exempted us from calibrating the WPRs. Finally, it is to be pointed out that, in our method, we also use the sign of the balloon humidity gradient to determine the sign of $M$.

## 3 Experiments, sites, instruments and radar data processing

### 3.1 Field experiments, measurement sites, instruments and radar data processing

Data were collected during three field experiments characterized by drastically different atmospheric conditions. The first experiment, the Boundary-Layer Late Afternoon and Sunset Turbulence (BLLAST) (Lothon et al., 2014), took place during a typical summer period in June 2011, at the Lannemezan Atmospheric Research Center (43.13°N, 0.13°E, elevation 595 m) at the Pyrenean foothills, and was characteristic of fair weather convective boundary layers at mid-latitudes. The second campaign is the first Special Observing Period of the Hydrological cycle in Mediterranean Experiment (HyMeX SOP1), which took place over the western part of the Mediterranean basin during autumn 2012 (Ducrocq et al., 2014). In this case the radar was installed in an atmospheric 'supersite' located in Candillargues (43.6°N, 4.07°E, elevation 2m) in the proximity of the seaside. The aim of the experiment was to study the upstream dynamical conditions linked to the initiation of strong rainfall events inland. The preferred situations were those when warm, moist and unstable air masses were advected from the sea. The third experiment was the HyMeX SOP2 experiment which was held during winter 2013, to study the mechanisms of air-sea exchanges in case of strong offshore winds (Estournel et al., 2016). The radar site was the same as for HyMeX SOP1.

### 3.2 Instruments

During these three experiments, intensive radiosounding (RS) operations (3h- or 6h-spaced) were performed with the purpose to monitor the atmospheric diurnal cycle. MODEM M2K2 and Vaisala RS92 (OYJ DigiCORA V3.64 / RS92-SGP) radiosondes were used for BLLAST and HYMEX respectively. The accuracy of the RS92 humidity measurements has been assessed by Miloshevich et al. (2006), based on the comparison of these measurements with those simultaneously performed by a reference sensor of known abolute accuracy (a cryogenic frostpoint hygrometer) deployed on the same balloon. In the low troposphere, as considered in the present study, they found that the mean accuracy in the relative humidity measurements (with respect to the absolute sensor measurement) is always lower than 5 %. In 2010, the World Meteorological Organization conducted a new intercomparison experiment in China (Nash et al., 2011). According to these authors, Vaisala RS92 version tested in China showed a systematic error of less than 2 % and a random error of $\simeq$ 5 % in relative humidity measurements in daytime and nighttime, from the surface to the low stratosphere, in clear-air or cloudy conditions. During this experiment, the MODEM M2K2 radiosonde was also compared to a set of different radiosondes, including the Vaisala RS92. According to Nash et al. (2011), MODEM nighttime measurements had large positive biases (larger than 10 %) for most of the time in the lower and middle troposphere. MODEM radiosondes were also found to suffer from evaporative cooling when emerging from a cloud layer, and to overestimate relative humidity by 6 % at night, for relative humidities in the range 90-100 %, i.e. in cloudy air. Luckily the BLLAST measurements, in contrast with the HyMeX observations, were systematically carried out in clear air, which mitigated the uncertainties in the MODEM measurements.

WPRs in the BLLAST and HyMeX were deployed by the Centre de Recherches Atmosphériques (Laboratoire d'Aérologie) and the Centre National de Recherches Météorologiques (Météo-France), respectively. Both profilers are 5-beam model PCL 1300 manufactered by Degreane. A detailed description of the WPRs, their main working parameters and the processing methods are provided in Saïd et al. (2016). Both radars were operated almost continuously at both sites over long periods (exceeding 18 months). For the purpose of this work, we will concentrate on the data collected from 19 June to 6 July 2011 during BLLAST, from 13 September to 5 November 2012 during HyMeX SOP1 and from 1 February to 15 March 2013 during HyMeX SOP2. Two operation modes were considered. The first mode (low mode), associated with a pulse length of 0.5/1 $\mu$s, sampled the low troposphere from 75/150 m AGL to 5/5.7 km AGL (for BLLAST/HyMeX respectively). The second mode (high mode) was specified for higher altitude sampling: from 150 m to 8 km AGL and a pulse length of 2.5 $\mu$s for both experiments. The vertical resolution was 75 m/150 m (for BLLAST/HyMeX respectively) in low mode and 375 m in high mode. The high mode was oversampled and provided data every 150 m. The interpulse period (IPP) was 40/45 $\mu$s (for BLLAST/HyMeX respectively) in low mode and 80 $\mu$s in high mode for both experiments. The radar beam was steered into five directions: one vertical and four oblique directions at zenith angle of 17° and 90°-spaced azimuths. The beam width was 8.5°, narrow enough to enable accurate measurements of the Doppler spectral width in the low troposphere.

In the frame of HyMeX-SOP1, the ground-based University of BASILicata Raman lidar system BASIL (Di Girolamo et al., 2009) was deployed in Candillargues and operated from 5 September to 5 November 2012, collecting more than 600 h of measurements, distributed over 51 measurement days and 19 Intensive Observation Periods (Di Girolamo et al., 2016). BASIL makes use of a frequency tripled Nd:YAG laser source, emitting pulses at 355 nm, with a single pulse energy of 500 mJ and a pulse repetition frequency of 20 Hz (average power at 355 nm: 10 W). The receiver consists of a Newtonian telescope (primary mirror diameter: 45 cm, f/2.1). The major feature of BASIL is represented by its capability to perform high-resolution and accurate measurements of atmospheric temperature and WVMR, both in daytime and nighttime, based on the application of the rotational and vibrational Raman lidar techniques, respectively (Di Girolamo, 2004; Di Girolamo et al., 2009). Besides temperature and WVMR, BASIL can also provide measurements of particle backscatter, extinction and depolarization at several optical wavelengths. Based on an integration time of 5 min and a vertical resolution of 150 m (which are the resolutions of the lidar data used in this paper), the typical daytime precision in WVMR measurements is 0.2 g kg$^{-1}$ up to 3 km and 0.3 g kg$^{-1}$ up to 5 km, while the typical nighttime precision is 0.05 g kg$^{-1}$ up to 3 km and 0.005 g kg$^{-1}$ at 10 km (Di Girolamo et al., 2016). During HyMeX-SOP1, BASIL measurements of WVMR were calibrated based on the comparison with simultaneous radiosondes (the RS mentioned above) launched from a facility located approximately 100 m away from the lidar. A mean calibration coefficient was estimated by comparing BASIL and radiosonde data at all times when BASIL was running (approximately 50 comparisons).

### 3.3 Radar data processing

The radar time series were coherently averaged to reduce the computing time while preserving signal detectability. The number of coherent integrations (NCI) was calculated for each cycle of 10 beams (5-beam steering in two modes), according to the windspeed measured during the former cycle, to optimize the Nyquist interval. 128-point Fourier transforms of the finite time series were applied to obtain radial velocity spectra. Finally, an incoherent integration of 30 successive spectra was made to improve the signal detectability. In case of rainfall, IPP was enlarged, NCI changed and backscattered power reduced, to avoid second trace echoes or saturation. This first step in raw data processing was made with the software provided by the manufacturer and implemented in the radar sites. One full cycle was achieved every 4 to 5 minutes (according to NCI) and represented 12 to 15 minutes observations.

The second step, called consensus, was processed in real-time and also post-processed at the Laboratoire d'Aérologie. The purpose of the consensus data processing is to determine the meteorological spectral peak among the four more powerful peaks of the Doppler spectra at each range gate. The method is fully described in Saïd et al. (2016). Special care was devoted to the separation between the meteorological peak and ground clutter echoes or the separation of individual echoes from a multiple-echo peak. This was decisive to provide an accurate spectral width of the Doppler peak, used to compute the dissipation rate of turbulent kinetic energy, $\epsilon$. Furthermore, special tests were performed to separate clear air spectra from precipitation spectra, using information from the four moments of the vertical velocity. Finally, we flagged out manually in the data post-processing the spectra disturbed by birds, that were frequent at night during the fall and late winter seasons of HyMeX, which coincided with migration periods.

### 3.4 Processing of the dissipation rate of turbulent kinetic energy

The dissipation rate of turbulent kinetic energy $\epsilon$ was computed according to the method and coefficients proposed by Jacoby-Koaly et al. (2002). Following Doviak and Zrnic (1984), Hocking (1988), Gossard et al. (1998) and White et al. (1999), they determined $\epsilon$ through the estimation of the broadening of the Doppler spectrum peak. The broadening of the spectrum had also to be corrected to contributions due to shear, to the antenna beamwidth and to the filtering effects of the Doppler spectrum. We chose to derive $\epsilon$ from a combination of the estimations obtained from the vertical velocity spectrum with the median of

Atmos. Meas. Tech. Discuss., https://doi.org/10.5194/amt-2017-265
Manuscript under review for journal Atmos. Meas. Tech.
Discussion started: 8 September 2017


the estimations obtained from the oblique velocity spectra. This method had been previously assessed by Jacoby-Koaly et al. (2002).

### 3.5 Radar calibration

Both radar were calibrated according to the method proposed by Campistron and Réchou (2012) and improved by Campistron et al. (2013). The calibration is based on the comparison between rain rate measured by the profiler and raingauge at the ground. The height of the radar data is taken as low as possible considering signal saturation, receiver linearity, and ground clutter. Usually the best level is found around 600 m AGL. Long lasting stratiform precipitation periods were chosen to avoid the presence of strong vertical air velocities. Also high relative humidity periods were selected to minimize rain modification during its fall.

Following Ulrich (1983), Campistron et al. (2013) assume that the drop size distribution of the rain follows a gamma function with two parameters that have to be determined. The drop fall speed in still air can be related to the droplets' diameter taking into account the change of density with height (Atlas et al., 1973; Foote and Du Toit, 1969). The parameters of the gamma distribution can be obtained using the mean vertical velocity and the radar reflectivity factor (Chu and Su, 2008). Finally the rainrate is derived by integrating the droplets' distribution over the diameter interval supposed to extend from zero to infinity.

During each rainfall event selected for the calibration, the radar constant was modified until the best agreement was found between raingauge and radar measurements. An average of the results was retained as the final calibration constant. As said before, the WPRs used in the framework of BLLAST and HyMeX had provided in fact longer dataset than the datasets we refer to for the present work. That is why we had no difficulty to find several stratiform conditions to achieve the calibration. The calibration was done for the BLLAST and HyMeX radars in low mode, and for the BLLAST radar also in high mode. For each radar and each operation mode, the variability of the calibration coefficients $K$ induced by the calibration method never exceeded 12 %, which is small relative to the variability of the coefficients $\alpha^2$ that will be discussed further on (cf. Sect. 4.3).

### 3.6 Data conditioning for the humidity gradient retrieval

During BLLAST, the balloon took around 4 minutes to cross the ABL whose top level was situated at level 2000 m ASL (1400 m AGL) on average. Within the ABL, the wind remained weak (around 4 m s$^{-1}$) which corresponded to the preferred conditions for the experiment (clear air, anticyclonic conditions). A nocturnal low level jet sometimes occurred at night, but it was seldom stronger than 6 m s$^{-1}$. During the first 4 minutes, the balloon drifted horizontally by 1 km from the release site, located nearby the radar site (150 m). The balloon reached the typical maximum height of the BLLAST radar soundings (4 km) in 17 minutes (from the release), which corresponds approximately to three full cycles of the profiler. For the humidity gradient comparison we used therefore 15 minutes of radar data, during which the balloon drifted horizontally between 5 and 15 km from the radar site, according to the wind conditions in the free troposphere. At a level of 2 km, the horizontal coverage of the radar observation was as small as 625 m, while it was twice as large at the height of 4 km.

During HyMeX SOP1 and as said before, the lowest atmospheric layers were mainly characterized by marine conditions, with southerlies or easterlies reaching 10 to 20 m s$^{-1}$ in the lowest 1-2 km (AGL and ASL). At this time of the year (fall season), the conditions were not propitious for sea-breeze development and mixed boundary layers had few opportunities to develop. Over 1 or 2 km, the wind conditions changed to the typical westerlies of mid-latitudes. The windspeed was never stronger than 25 m s$^{-1}$ at the height of 5 km, which was the maximum height reached by the radar echoes during SOP1 (moister conditions than during BLLAST, so better detectability of the echoes). The balloons typically took 5.5 and 14.5 minutes to reach the heights of 2 km and 5 km, respectively. 14.5 minutes correspond to almost three full cycles of the radar. Due to the shear in the wind direction, the maximum drift of the balloon during its ascent was 10 km from its release point.

The radiosonde data were averaged by slices of 75 or 150 m (according to the radar vertical resolution), centered on the radar gates levels. This revealed to be a better choice than interpolating the radar data, but could yield some slight discrepancies in case of sharp humidity gradients.

We carefully interpolated the radar measurements to fill some gaps in the data. Profiles with gaps larger than 750 m were excluded from further analysis. Second order radar estimations (vertical shear and $\epsilon$) were smoothed to avoid sharp local derivatives. Since 1274-MHz WPRs are sensitive to both turbulence and raindrops, individual profiles were also checked to remove profiles contaminated by precipitation echo (essentially during HyMeX SOP1). However, we kept the profiles for which the precipitation echo was confined at a limited number of levels and the measured vertical velocity did not exceed 0.5 m s$^{-1}$. These conditions were frequently encountered during HyMex SOP1 when virga (rainfall that does not reach the ground) appeared, due to the large evaporation rates of the warm lower layers, at the end of the summer season.

## 4 Radar humidity profiles versus radiosonde profiles

### 4.1 Some adjustments to improve the method

Before providing detailed humidity profiles between successive radiosoundings, we had to check how the humidity profiles retrieved by the radar were consistent with the initial radiosonde profiles. This took the longest time to perform since it required several adjustments.

The first adjustment was already mentioned in section 2. We solved the sign ambiguity on $M$ (since the radar provides $M^2$), by assigning to $M$ the sign provided by the RS observations (Eq. (6)). Figure 1 illustrates the change in the $M$ and $q$ profiles from before and after the correction. In this and the following figures, when not differently specified, with the term of humidity profile we intend to represent the water vapor or humidity mixing ratio profile. We had initially assigned a negative sign to $M$, which had revealed to be relevant for most of HyMeX SOP1 conditions, where the source of humidity is close to the surface (maritime air masses) and decreases with the height. There were however situations, either during BLLAST or HyMeX, when drier layers disrupted this negative gradient. We show an example from BLLAST in Fig. 1. In Fig. 1 (a), $M$ is computed from Eq. (6) for the RS observations (red line) and extracted from Eq. (15) for the radar (black line), assuming a constant negative sign on the whole profile. The resulting radar humidity profile shown in Fig. 1 (c) rapidly deviates from the observed profile (RS profile) and maintains the deviation, in both the upper or lower parts of the profile. The downward and upward integrations computed to retrieve $q$ are connected at Hlim = 1745 m, which corresponds to a maximum in the radar reflectivity profile and to a change in the observed humidity profile. The approach to select this level will be discussed later on. The successive changes in the sign of $M$ are taken into account in Fig. 1b. The resulting radar humidity profile is clearly improved (Fig. 1 (d)). The thin red lines in Fig. 1 (c) and (d) represent the humidity retrieval as obtained from the integration of $M_{RS}$, after averaging the RS observations by slices of 75 m, to match the vertical resolution of the radar. The discrepancy between the two red lines can be considered as a systematic error associated with loss in vertical resolution linked to the 75 m averaging.

Occasional negative values of $q$ are put to zero especially during BLLAST when very dry layers were observed. Similarly, some unexpected large values of $q$ were put to the humidity saturated value provided by the RS. This occurred during HyMeX SOP1 when moist conditions were frequently encountered. This limitation enabled to minimize the error accumulation in case of divergence of the integration. We will provide illustrations of such situations in the following.

Another improvement consisted in testing different values of the Hlim level in case of relative maxima in the radar reflectivity profiles. An example is provided in Fig. 2. The $Cn^2$ profile in Fig. 2 (a) shows three peaks. The dominant peak at 902 m corresponds to the lower level of a virga, since the water vapor content observed with the RS is saturated (the red solid and dashed lines are superimposed in Fig. 2 (b)). The double integration of the radar data upward and downward to this level provides the radar profile of $q$ presented in Fig. 2 (b) (black line). Radar and RS profiles agree up to 1500 m, but above this level the radar profile deviates from RS. In this specific case the downward integration fails (below 3100 m). We recall that in the upper part of the profile, the integration is performed from 4800 m down to Hlim = 902 m. The combination of $Cn^2$, $\epsilon$ and shear measured by the radar fails in reproducing the discontinuity present in the RS profile between 3100 m and 2800 m. This may be due to the spatial heterogeneity of the air mass, but there is no specific ancillary information to prove it. Other computations are done, using the other peaks of the $Cn^2$ profile and considering Hlim = 1802 m and 3452 m. The best result is obtained when Hlim = 1802 m, which is the height of the second peak from ground. The result is illustrated in Fig. 2 (c). It shows a slight improvement of the agreement in comparison to results shown in Fig. 2 (b), although the divergence of the radar profile below 3100 m down to 2400 m is still obvious. The transition at 1802 m does not correspond to any marked transition in the RS humidity profile. This choice probably improved the result due to its central location in the profile.

Figures 2 (d) to (f) illustrate the results for the same profile, when the low mode is used instead of the high mode. In this case, the vertical resolution of the radar measurements is 150 m instead of 375 m. This can be checked on the $Cn^2$ profile in Fig. 2 (d), which is not as smoothed as in Fig. 2 (a). The agreement between the radar and RS profiles of $q$ is sligthly improved, but again not striking (Fig. 2 (f) compared with Fig. 2 (c)).

Finally, another issue was raised by the choice of the initial conditions. We constrained the value of $q_o$ to be equal to the RS observation at the same level. This level sometimes coincided with a level of sharp inversion, as illustrated in Fig. 3 (a) at 3000 m or in Fig. 3 (c) at 4400 m. This was frequently the case at the upper boundary during BLLAST since the range gate where the radar echoes vanished also coincided with a moisture inversion. So we rectified the initial value by hand, to avoid an accumulation of the error along the whole profile, as shown in Fig. 3, where the humidity profiles prior (left column) and posterior (right column) to the correction are compared. Note also that the upper boundary condition obtained from RS data and used for the integration of $M$ has been changed in Fig. 3 (d), which leads to an increased agreement between the observed and calculated RS humidity profiles (red thin and solid lines). We are well aware that this hand-made correction could not be applied for an operational purpose, but attempts to ingest this correction procedure in a dedicated algorithm are currently underway.

The previous illustration revealed one major limitation of the approach used to retrieve the humidity profile. In fact, in case of multiple strong inversions in the low troposphere, as those observed in Fig. 3, the method failed since we had no possibility to distinguish between the different sublayers. In this specific case, the second sharp inversion is at the upper border of the radar profile since the dry air above 3100 m or 4400 m did not produce backscatter echoes. We could therefore avoid illustrating the documentation of the profile over these levels. By contrast, in some other cases where the radar height range is larger as during HyMeX, the radar had difficulties to accurately retrieve successive strong inversion layers.

### 4.2 Comparison between the RS and radar retrieved humidity profiles

Results are presented in Fig. 4 to describe the atmospheric conditions observed during the three experiments and to illustrate the humidity profiles obtained with the WPR at the same location and time as the RS launching. We wish to insist here on the fact that the results illustrated in this figure required all the adjustments described in the previous section.

Panels (a) to (g) illustrate the moist conditions encountered during HYMEX SOP1 in the lower layer and various humidity inversions, with variable steepness, that were usually well retrieved by the WPR. Panel (c) provides an example of the necessity to limit the humidity content to its saturated value between 2100 and 3100 m. Almost all humidity profiles show at least one portion that is close to saturation. This is usually well retrieved by the radar, except in the case of panel (f), where the radar estimation degrades from the initial height of the upper integration (4000 m) down to 1052 m. Note also that the humidity jump in the radar profile between the low layer (7.8 g kg$^{-1}$) and the upper layer is essentially due to the detection of a maximum in the $Cn^2$ radar profile (at 1052 m). The connection of the radar profile between both parts of the sounding helps providing a somewhat correct estimation in the lower layer. The faulty estimation by the radar in the upper part of the profile comes from an overestimation of $M$: $Cn^2$ is still strong just above the inversion, where a positive sign has to be assigned to the corresponding $M$. This led to an overestimation of $\alpha^2$ in the upper part of the profile. In this case the failure of the radar is due to the combination of a sharp inversion capped by a positive slope in the humidity profile. The use of the high mode did not improve the humidity retrieving either. Panel (g) shows another case where the radar failed in properly retrieving the humidity profile, for reasons similar to those considered above.

Among the BLLAST profiles, we chose the illustrations of panels (h) to (j), observed at 11:04 UTC, 17:50 UTC and 22:54 UTC on 19 June 2011 to show how the vertical humidity profile was likely to evolve during the day. In the late morning (panel (h)), a thin dry layer is present just below 2000 m. It is clearly visible in the radar data, even if the latter are moister. The large values of $Cn^2$ measured by the radar at this time are not associated with the boundary layer height (1500 m). It is an area where the strongest wind shear and humidity gradient are observed. This wind shear is between the slope wind of the low layers (weaker than 5 m s$^{-1}$) and the synoptic wind above (not shown). This situation was frequently observed during BLLAST. The dry layer vanished at 17:50 UTC (panel (i)), probably as a result of the subsidence of the upper air, down to about 1700 m, while the ABL has turned a little moister (5.8 to 6.4 g kg$^{-1}$), but not any deeper (due to the subsidence). The conditions evolved again after the sunset (panel (j)) and the reversal of the breeze. The moisture slightly increased in the lower layer, with the 1100 m-deep down slope breeze. The radar correctly retrieved the evolution of the humidity profile during the day. Note the variability in the $\alpha^2$ values obtained in the lower layer. From values of 0.1094 and 0.0247 observed in the daytime mixed layer, it increased to 5.0183 in the nocturnal stable layer, showing a potential influence of the stability conditions (see the related discussion in section 4.3).

The last examples shown in panels (k) and (l) are representative of the weather conditions encountered during HYMEX SOP2. We chose on purpose the profiles obtained with the high mode for which the detection is easier than for the low mode (due to the high mode longer pulse length and longer inter pulse period). During this winter months and offshore wind events, the air is very dry in altitude (only 0.6 g kg$^{-1}$ in panel (l)) and the radar has difficulty to find echoes, so the vertical range of the low mode is seldom higher than 2 km, sometimes even only 1 km. The vertical profile of temperature (not shown) is stable very close to the surface (up to 150 m) on 12 February 2013 at 18:21 UTC (case (k)), but neutral above in a well mixed layer with a vertical extent of 2100 m due to the dynamic turbulence generated by a strong continental wind (12 m s$^{-1}$), channeled by two mountain chains. The temperature profile is also neutral on 24 February 2013 at 08:35 UTC (case (l)) in a well mixed ABL (potential temperature is around 0°C) up to 1500 m. The windspeed increases from 10 m s$^{-1}$ at 500 m to 18 m s$^{-1}$ at the ABL top. The discontinuities observed in the $Cn^2$ at 2102 m and 1802 m (panels (k) and (l), respectively), correspond to a slight decrease in the humidity profile. In contrast a strong temperature inversion occurs at 2100 m on 12 February (panel (k)), whereas there are two temperature inversions on 24 February (panel (l)), at 1500 and 1900 m. In both cases, the large $Cn^2$ values yielding Hlim, probably demarcate the presence of a thin layer, the so-called bright band, where melting ice is mixed with water droplets and $q$ is saturated. However, the discontinuities in the humidity profiles are weak in both cases, due to the fact that the air is dry at the surface since it has traveled a long way over continental areas, with several opportunities of losing humidity, especially under those low temperature winter conditions. These profiles are representative of the HyMeX SOP2 conditions. In most cases, the weak humidity variation with the height and the limited vertical range made easier the retrieving of the humidity profiles from the WPR data since the profiles were almost linear apart the $Cn^2$ discontinuity.

We gathered in Figure 5 the results of the comparison between the radar estimation of the humidity profile and the observed RS humidity values for the three data sets in low mode. Panels (a), (c), (e) and (g) show the scatterplots of the radar vs. the radiosonde data, and panels (b), (d), (f) and (h) show the vertical profile of the deviations between the radiosonde and the radar data, all of them obtained from low mode data. The red line in the scatterplots represents the linear regression line drawn from the data, which can be compared to the slope 1:1 black line. HyMeX SOP1 data, the most numerous in terms of number of profiles, were split into two graphs. The vertical resolution of the BLLAST WPR measurements is three times higher than the one characterizing HyMeX measurements, which explains the larger sample size in Fig. 5 (a). The results are also summarised in Table 1, where the high mode has been added.

The best results are clearly those obtained during HyMeX SOP2, since the correlation coefficient is exceeding 0.93, the mean bias is 0.04 g kg$^{-1}$ or smaller and the mean standard deviation is 0.18 g kg$^{-1}$ or smaller. We mentioned previously that the reason for these successful retrievals is linked to the limited variability of the humidity content and the small vertical range of the radar data associated with dry conditions. So we cannot rely upon this example to assess our method. In most other cases, with the exception of the BLLAST data in high mode, the correlation coefficient exceeds 0.8, the slope of the regression lines is close to unity, the mean bias is equal or smaller than 0.24 g kg$^{-1}$ and the standard deviation is not exceeding 1 g kg$^{-1}$ (Table 1).

The drastic error increase appearing in Fig. 5 (panel (b)) above 4000 m is due to the correction in the initial conditions that we discussed in section 4.1 and illustrated with Fig. 3. For most of the BLLAST profiles, the initial conditions for the radar had to be shifted to larger values, so that the profiles were correct just below the strong inversion capping the range of the radar observations. We made the choice of discarding the upper humidity inversion (occurring at 3000 m in Fig. 3 (panel (b)) or 4400 m in Fig. 3 (panel (d)) for instance), since the radar was not able to document it correctly, given the lack of data over the inversion. We decided then to reprocess the data shown in Fig. 5 (panels (a) and (b)) and to restrict the comparison to the vertical interval 845-4000 m. The results are of course improved: the correlation coefficient increases from 0.83 (Fig. 5, panel (a)) to 0.87 (Table 1), and the mean bias is now -0.07 g kg$^{-1}$ (Table 1) instead of -0.35 g kg$^{-1}$ (full data set, Fig. 5, panel (b)).

We identified the reason why the BLLAST dataset gave poorer results in high mode than in low mode. In high mode these are 0.73, 0.36 g kg$^{-1}$ and 1.19 g kg$^{-1}$ for the correlation coefficient, mean bias and standard deviation, respectively (Table 1). These relatively lower quality results are due to the difficulty of the radar, when operated in high mode (the vertical resolution is 375 m), to detect thin layers as the dry one shown between 1700 m and 2000 m ASL in Fig. 4 (panel (h)). In this case, the radar in low mode indicates two $Cn^2$ transitions peaking at 1670 m and 1970 m whereas the high mode provides only one larger peak peaking at 1645 m (not shown). Even if the low mode retrieval of the thin dry layer is not perfect, the high mode is worse. The underperformance of the high mode can be explained by the occurrence of this kind of drier (or moister) thin layers, that were frequently observed during BLLAST, at the boundary transition between the slope wind and the synoptic wind.

The other results in Table 1 do not exhibit an outperformance at any of the two modes. Concerning the variability of the error and its standard deviation along the vertical, we cannot draw any general conclusion even if the HyMeX results seem to be better (smaller bias, smaller standard deviation) above 2500 m (Fig. 5, panels (d) and (f)). The bias remains small and similar for BLLAST within the whole profile, below 4000 m.

To conclude, we consider that the method we propose yields good radar profiles to start the processing at a finer time resolution. Before getting the intermediate profiles, let us examine the variety of calibration coefficients $\alpha^2$ that were obtained for the three data sets.

### 4.3 Variability of the calibration coefficients

With the aim of comparing the calibration coefficient $\alpha^2$ in Eq. 15 to the coefficients found in literature and studying its variability relative to the stability conditions, we first considered the coefficients within each dataset, which enabled to avoid possible issues about the radar calibration. According to Eq. 14 and 15 and considering the same WPR, the variability in $\alpha^2$ should reflect the variability of the ratio of the two outer scales $\frac{L_w}{L_\phi}$. Gossard et al. (1998) expected this quantity to be dependent on the stability conditions, at least inside the ABL, where the turbulence is homogeneous. Small ratios should occur under stable conditions, which would correspond to large $\alpha^2$ values, and the opposite behavior under unstable conditions.

To check this hypothesis, we used the radiosonde data to get an estimation of the stability conditions based on the gradient Richardson number :

$$Ri = \frac{g}{\theta_v} \frac{\frac{d\theta_v}{dz}}{\left[\left(\frac{du}{dz}\right)^2 + \left(\frac{dv}{dz}\right)^2\right]} \tag{18}$$

where $\theta_v$ is the virtual potential temperature and $u$ and $v$ are the horizontal components of the wind. We chose the BLLAST dataset, since summer conditions provide the largest range of stability conditions. Figure 6 shows the calibration coefficients obtained from the BLLAST dataset in low mode as a function of the stratification with a differentiation of the lower part and upper part of the profiles, located below and above Hlim, respectively. The colorscale indicates the hour of the day. During the convective period of the day, the lowest portion of the profiles is expected to correspond to a mixed ABL, with Richardson numbers potentially negative in the surface layer, and close to zero above. The corresponding calibration coefficients can be clearly identified in the bottom left corner of Fig. 6. Smaller values (below 0.01) are observed under unstable conditions, in accordance with Gossard et al. (1998). However a significant number of the coefficients corresponding to unstable conditions are also located in the range 0.03-0.5, where most of the coefficients of the lower layer can be found (the logarithmic mean of $\alpha^2$ in the lower layer is 0.11). On the contrary, nighttime coefficients measured within the lower layer (dark blue and orange circles) are preferentially large (>0.5), while the Richardson number can vary, but usually is close to or larger than 0.25, the critical Richardson number, indicating stable conditions. As expected, the upper layers are slightly or clearly stable (squares), but there is no tendency for $\alpha^2$ relative to the stratification intensity. In this case the logarithmic mean is 0.16, not far from the value observed in the lower layer. According to VanZandt et al. (1978), the variability of the coefficients in the upper part of the profiles is linked to the variation of the 'filling factor' and depends on the lapse rate of the free troposphere. Anyhow, this variability (the squares span roughly two orders of magnitude) is less marked than the variability due to the stability conditions of the low layers (the circles span four orders of magnitude). The average of the whole set of calibration coefficients for BLLAST yielded a value of 0.13, which is close to the lower boundary of coefficients [0.26-1.11] proposed by Gossard et al. (1998).

The BLLAST coefficients obtained with the high mode are not presented since we estimated they are not representative, especially in the lower part of the profiles. First, the average of the transition levels (Hlim) is 1193 m AGL in high mode versus 928 m AGL in low mode, and the distribution is clearly shifted towards higher Hlim values in high mode, which means that the transition level is certainly higher than the boundary layer top in most cases. In second place, we obtained rather large values of the coefficients (6 coefficients larger than 10) for the lower part of the profiles, that we attribute to the poorer vertical resolution in high mode in an area of sharp variations of the humidity.

The same analysis was applied to the HyMeX datasets from which no significant result arose, neither during SOP1 nor SOP2 (not shown). Unstable conditions were too occasional to show any tendency. Usually, the upper layer exhibited a stronger stratification than the lower layer, but the calibration coefficients varied irrespectively of this variation. Although the HyMeX radar was calibrated (in low mode), the coefficients that were obtained during SOP1 were one third the BLLAST coefficients.

We artificially shifted the HyMeX calibration coefficients (by multiplying them by 3) to make the logarithmic average match, so to be able to compare the variability.

Results are illustrated in Fig. 7 in terms of upper layer versus lower layer $\alpha^2$ coefficients. As seen before, due to the variability in stability conditions, BLLAST is characterized by a larger span of lower layer coefficients. HyMeX SOP1 and SOP2 coefficients span roughly two orders of magnitude in the lower layers and two orders of magnitude in the upper layers on each side of the 1:1 line. The identification of the convective period (represented by the crosses) confirms that HyMeX observations were not performed under unstable conditions (that would have yielded lower coefficients), even during the daytime period. The main conclusion we can draw from these results, coming primarily from the BLLAST data, is the necessity of distinguishing between the mixed layer and the free troposphere in case of unstable conditions in the low troposphere. Fig. 7 also suggests that the 'filling factor' proposed by VanZandt et al. (1978) for the upper layers do not vary that much. This explains why some authors obtained satisfying results by using a constant coefficient with VHF-band WPRs when sensing this portion of the atmosphere.

We experienced the effect of using a constant calibration coefficient on the BLLAST dataset in low mode. We successively used 0.13, the average of the BLLAST coefficients and 0.44, the average proposed by Gossard et al. (1998). The correlation coefficient of the linear regression dropped from 0.87 to 0.73 and then 0.56 when passing from a varying to a constant calibration coefficient. The bias changed from -0.07 to 0.04 (not much!) and then increased to 0.77 g kg$^{-1}$. The mean standard deviation increased from 0.82 to 1.16 and 1.65 g kg$^{-1}$.

We propose an explanation to the different results obtained in terms of calibration coefficients during HyMeX SOP1 (0.04 on average) and BLLAST (0.13 on average). We recall that both radars were calibrated. We assume that we can rely on this calibration since i) values of $Cn^2$ determined for BLLAST in high mode are similar to those obtained in low mode and ii) the two calibrations, based on the rain gauge measurements, are independent. During HyMeX SOP1, as clearly highlighted by the examples shown before (Fig. 2, panels (c) and (f); Fig. 4, panels (c), (d), (e) and (g)), atmospheric thermodynamic conditions were often close to saturation. Although we discarded the rainy radar profiles when the rainfall affected the whole air column, it is likely that virga or pockets of rainfall may have locally increased the radar $Cn^2$, which implies a decrease in $\alpha^2$ (we verified that the Doppler spectra had no additional variability as a result of the variability in the water droplets falling speed, which can alter $\epsilon$). We checked the distributions of $Cn^2$ for the 3 datasets and found that the logarithmic averages of $Cn^2$ (close to the median values) gave 1.4, 31 and 1.0 $10^{-14}$ m$^{-2/3}$, for BLLAST, HyMeX SOP1 and HyMeX SOP2, respectively, which confirms the former hypothesis of higher $Cn^2$ values (and consequently lower calibration coefficients) for the moist conditions during HyMeX SOP1. This disturbance could be considered as a limit in the application of the method we propose, since the conditions of clear air turbulence required for the application of Eq. 13 would not be totally fulfilled. However we maintain that, based on the good results we obtained (see Fig. 5, panels (c) and (e)), the method can be successfully applied to HyMeX SOP1.

## 5 Continuous humidity monitoring between radiosonde observations

### 5.1 Method

Our objective in this section of the paper is to check whether radar data can be successfully used to describe the detailed structure of the low troposphere between two successive radiosoundings, even if the latter are 6 or 12 h-spaced. The two bordering soundings, called RS1 and RS2, are used as initial and final conditions. We first retrieved the radar humidity profiles closest to RS1 and RS2 on the bases of the application of the algorithm described in the previous sections. The algorithm provides the values of Hlim and the calibration coefficients at the launching times of RS1 and RS2. RS1 and RS2 also provided the initial and final bottom and top border conditions for $q$, which we interpolated at the radar times (every 15 minutes). Pressure and temperature values were also interpolated at the times between RS1 and RS2 (at all levels) to provide $\theta$ and $P$ present in Eq. 12 and also to constrain $q$ to the humidity saturated value based on the interpolation of the RS data at the same time and level. In addition, the sign of $M$ at each level was taken as the sign of the RS1 humidity gradient at the same level for the first half of the period separating RS1 and RS2 and as that of RS2 for the second part of the period. Finally, the radar calibration coefficients $\alpha^2$ were time-interpolated. In contrast, values of Hlim obtained from the radar data at the launching times of RS1 and RS2 were not interpolated. The radar provided an updated value of Hlim and an updated vertical profile of $M^2$ every 15 minutes (through new $C_n^2$, shear stress and $\epsilon$ profiles). Ultimately, using Eq. 12, the vertical profile of $q$ may be retrieved at a fine time resolution of 15 minutes. The choices for the parameters just described are summarized in Table 2.

In case of several values of Hlim due to the presence of several peaks in the $C_n^2$ profile obtained at time $t$, a continuity criterium was used to select the appropriate value. This criterium was applied to a variety of HYMEX case studies, which frequently showed several inversion layers. By contrast, the $C_n^2$ profiles observed during BLLAST exhibited a marked isolated peak that could be directly taken as Hlim.

### 5.2 Some results

A first example of the results obtained during HYMEX is shown in Figure 8. RS1 and RS2 are 6 hours-spaced and were chosen to illustrate a case study, on 24 September, when the moist lower troposphere dries and a mixed boundary layer develops. The RS1 humidity profile at 03:14 UTC is close to saturation from 500 m up to 2000 m (Fig. 8, panel (a)), whereas the RS2 profile at 09:00 UTC is drier and shows a mixed layer with a depth of 1350 m and a constant $q$ value of 8.4 g kg$^{-1}$ (Fig. 8, panel (b)). The humidity profiles retrieved by the radar between 03:14 and 09:00 UTC are represented with thin solid lines in Fig. 8 (panel (c)), with the time being color coded. The dashed lines are the corresponding saturated profiles calculated from the profiles of $P$ and $T$ obtained by interpolating the data from the two RS. The radar profiles gradually dry in the lower levels and a mixed boundary layer develops from 07:14 to 09:00 UTC, accompanied by a decrease in air temperature (with a consequent decrease of the saturated mixing ratio between RS1 and RS2 in Fig. 8, panel (c)). In fact, the weak low-level wind, which had blown from the south in the early morning, turned gradually to north-westerly wind between the sunrise (around 05:00 UTC) and 06:14 UTC (not shown). The mist marine layer was then replaced by a continental, cloud free boundary layer that could easily develop due to an increase in the wind strength (15-20 m $s^{-1}$) and to a larger surface-air temperature contrast. The radar was particularly helpful to detect the top of the mixed layer.

In Figure 8 (panel (d)), we compare the radar humidity profiles (solid lines) to the 15 min-averaged profiles obtained with the lidar at the same times (crosses) and to the humidity profiles calculated from a linear interpolation of the RS1 and RS2 profiles (dashed lines). The first four lidar observations (between 03:14 and 04:59 UTC) are attenuated above 750 m because of the presence of a cloud layer. In fact, atmospheric particles can lead to antagonistic effects on the lidar beam: few and scattered particles may lead to an increase of the backscattered radiation, whereas dense particle ensembles, as those found in a thick cloud, are usually characterized by large optical thicknesses (>1-2), which translates into laser beam attenuation overwhelming particle backscatter. In the early morning, the sharp decrease of the lidar signal above 750 m in Fig. 8 (panel (d)) clearly reveals the base of a thick cloud at 750 m. As the air dries up with the time the lidar recovers its capacity to cover the lower troposphere and the final lidar humidity profiles are very close to the RS2 and radar profiles.

The representation in Fig. 8 (panel (d)), hardly enables to distinguish between the radar humidity and the humidity calculated from the RS interpolation. That is why we preferred to show the same results with height-time cross-sections of WVMR (Fig. 9). In this figure, we highlight with black dots the levels characterized by saturation conditions. Due to the difficulty to rely on the lidar humidity profiles measured under saturated conditions, we superimposed on the lidar WVMR map in Fig. 9 (panel (a)), the dots obtained with the RS data (the same as those in Fig. 9, panel (c)). The thick cloud remains over the lidar until 05:00 UTC. Simultaneously, the radar detects saturated values of WVMR (Fig. 9, panel (b)), revealing that the cloud is probably a virga. After a short period of clear air, another virga is advected over the measurement site between 05:30 and 06:30 UTC, with a base at 1100 m, as indicated by the lidar. This virga is also captured by the radar, with saturated values of WVMR from 1500 m to 2200 m or more, at 05:30 and 06:30 UTC. After 05:00 UTC the lidar shows WVMR values similar to those measured by the radar and the RS in the low layers, although the mixing of the boundary layer is best represented by the radar and probably the most likely since it results from an accurate measurement of the inversion height, well marked by the Hlim transition. The moisture retrieved by the radar exhibits a mixed boundary layer, whose depth increases from 500 m (07:00 UTC) to 1300 m (09:00 UTC) and dries with the time.

With the following example (case study on 23 September 2012 from HYMEX), we extended the time separating the two border radiosounding by choosing RS1 at 09:01 UTC and RS3 at 20:31 UTC. This enabled to use an intermediate RS at 14:58 UTC, called RS2, and to compute the radar profiles during three distinct periods, namely 09:01-14:58 UTC (panels (a), (d), (g) and (j) in Fig. 10, 14:58-20:31 UTC (panels (b), (e), (h) and (k)) and 09:01-20:31 UTC (panels (c), (f), (i) and (l)). The juxtaposition of the first two columns should give the third. As expected, this is clearly the case for the lidar (panels (d), (e) and (f)) but not so obvious for the interpolated RS (panels (j), (k) and (l)).

The RS bottom border conditions in Fig. 10 (panel (l)) do not recreate the drying that occurs at 500 m between 09:00 and 15:00 UTC (panels (a) and (j), 12 down to 7 g $kg^{-1}$) and the following moistening from 15:00 to 20:30 UTC. The saturated areas (black dots) in panels (l) or (j) and (k) are not consistent either. Remember that the dots in this row are those from the interpolated RS. In fact, the decrease in the WVMR at 500 m in panel (j) widens the gap to the saturation, especially as the saturation values climb due to the increase of temperature with time. In contrast, the low layers moistening from 15:00 to 20:30 UTC rapidly leads to saturation conditions, not at the surface where the air is warm, but a little higher at 1300 m (Fig. 10 (k) around 16:00 UTC). A deeper cloud layer appears around 18:00 UTC as testified by the RS interpolation in panel (k). The thickening of the cloud layer occurs later, around 19:30 UTC in panel (l). Consequently, a simple interpolation within the 12 h interval between RS1 and RS3 seems unrealistic since it does not reflect the proper daytime evolution of the low level boundary conditions. This also influences the saturation conditions at the mid-level.

The comparison with the lidar exacerbates the difficulty for the radiosoundings to describe the humidity fields under non steady atmospheric conditions. On 23 September, a strong convective line was active, far west to the site, extending from Iceland to the west of the Iberian Peninsula (this convective line finally crossed the measurement site during the following night). This frontal activity generated a pocket of moist air in the lower layers, that was advected by south-easterly winds (150° at 500 m) over the western Mediterranean sea, while it circumvented the Pyrenean mountains. Another pocket of moist air was situated to the east of the site, due some convective activity over Italy. Between these two areas of large WVMR, there was a pocket of drier air that moved according to the relative influence of the two convective areas on each side. Consequently, the measurement site, that was located in this area, encountered varying moisture conditions.

The lidar is well capturing the large variability in the humidity content characterizing the lower levels with large WVMR (13-14 g kg$^{-1}$) in the time interval 09:30-13:30 UTC (Fig. 10 panel (d)), as a result of the influence of the western convective line, and the drying of the lower layers in the time interval 13:30-20:30 UTC (Fig. 10 panel (e)), when the moisture pocket moved further to the west. The 09:00 UTC RS that was launched during a period of increasing moisture (12 g kg$^{-1}$ between 500 and 800 m), is not able to capture the whole increase (unfortunately the lidar data were missing at 09:00 UTC as indicated by the blue vertical stripe from 09:00 to 09:45 UTC in Fig. 10 panel (d)). Consequently the radar, whose initial conditions are based on the 09:00 UTC RS, fails in capturing the large humidity amounts characterizing the lower layers between 09:30 and 13-30 UTC (Fig. 10 panel (g)).

Between 13:30 and 17:00 UTC, the radar estimations below 1500 m are closer to the lidar measurements. Both instruments indicate a top level of the moist layer varying between 1200 and 1500 m (Fig. 10 panels (d-e) and (g-h)). Above this level, the lidar beam is extinguished by deep clouds. The detection of this transition level is facilitated, for the radar, by the fact of being marked by a large wind shear which favors the $Cn^2$ increase.

Between 17:00 and 18:30 UTC, the radar and the lidar both detect higher WVMR amounts in an intermediate layer between 800 and 1500 m or 500 and 1100 m, respectively (Fig. 10 panels (e) and (h)). Within this layer, the radar shows saturated values close to the levels where the interpolated RS WVMR values are saturated, but limited between 17:00 UTC and 18:30 UTC. The radar WVMR values are also consistent with the lidar values. Between 16:00 UTC and 18:30 UTC, the radar detects a virga in the 2000-2500 m layer (Fig. 10, panels (b) and (h)). Virga is also well visible in the particle backscatter field (not shown) obtained by the lidar. The particle backscatter data at 1064 nm are able to properly reveal both aerosol layers and cloud/precipitation particles. Specifically, hydrometeors evaporating/sublimating before reaching the ground are observed (as vertical thin stripes) between 17:30 and 19:00 UTC in the vertical region 0.5-1.2 km.

Finally, if we now consider the capacity of the radar to retrieve the WVMR variability during the whole period from 09:00 UTC to 20:30 UTC (Fig. 10, panel (i)), we must recognize that the radar fails to reproduce the lidar data (Fig. 10, panel (f)), with the exception of the transition level around 1400 m, between 13:00 UTC and 20:30 UTC. The virga mentioned previously is unfortunately not seen, probably due to the erroneous calibration coefficients imposed by the too large interval separating the two bordering RS.

The September 23 case study showed that, for changing conditions near the surface (that are not typical of a classical diurnal cycle evolution) and 12h-spaced radiosoundings, both the combined radar-RS algorithm and the simple time interpolation between two radiosoundings fail to reproduce the detailed structure of the humidity in the low troposphere, essentially because of a lack of documentation of the evolution of the humidity at the first radar gate. As said before, the data from a ground station would not have been helpful, due to the variability between the surface and the first radar gate (see for instance in panel (e) of Fig. 10). By contrast, when the time interval between the two RS was reduced to 6 h, the radar proved to be able to retrieve the WVMR amounts measured by the lidar and the presence of a virga in the intermediate layers.

Another example to illustrate the performance of the radar-based approach with respect to a RS interpolation and the lidar measurements is shown in Fig. 11. RS1 and RS2 on 26 September are 6h-spaced. Both show clear air and a regular reduction of the humidity content with the height (Fig. 11, (panel (c)). In fact, a burst of moister air occurred between the two RS at 03:00 and at 09:00 UTC, that is well observed with the lidar (Fig. 11, panel (a)), and partly retrieved by the radar (Fig. 11, panel (b)), with local saturated values. Even if the radar retrieval shows a few erroneous profiles (04:30, 05:30 , perhaps 07:00 and 07:30 UTC...), the radar documentation is necessary to detect the morning moistening of the air.

The last case study considered in this paper includes measurements carried out on 02 July 2011. It has been taken from the BLLAST experiment, to examine the evolution of a boundary layer in clear summer conditions associated with a moistening of the mid-layer capping the boundary layer. This is a typical situation observed during BLLAST, with a lower layer characterized by weak and easterly wind conditions topped by a layer characterized by an area of marked windshear (velocity and direction) associated with a drastic drying of the air. Usually, this situation takes place under anticyclonic conditions and is typical of the whole region (300 x 300 km$^2$, at least to the north of the Pyrenean mountains). The strong inversion at the top of the boundary layer is frequently holding for several hours and counters the mixed layer development, as a result of the strong subsidence linked to the anticyclone.

Fig. 12 shows the results for two overlapping time intervals of 02 July, i.e. 04:55-10:40 UTC (panels (a), (d) and (g)), 10:40-16:29 UTC (panels (b), (e) and (h)) and 04:55-16:29 UTC (panels (c), (f) and (i)). There was no lidar to compare the results during this experiment, so the only mean to assess the data is to check its consistency with respect to the RS interpolation. The radar profiles collected during the BLLAST experiment offered a good opportunity to apply the proposed method since they were most of the time, both in daytime and nighttime, characterized by a well marked inversion, corresponding to either a mixed or a residual boundary layer. The results presented in Fig. 12 are far less disturbed than the results shown previously for the HYMEX experiment, except for some individual profiles that can be identified by leaks of different colors (sky-blue leaks around 06:00 UTC between 1700 and 2200 m or green vertical spot around 08:00 UTC in panel (f) for instance). Panel (f) can be successfully compared with panels (d) and (e). The top of the residual/mixed boundary layer slightly oscillates between 1500 and 1600 m and is consistent with the RS interpolated value which remains at 1550 m.

However, the results retrieved by the radar show a tendency to accentuate the curvatures: the darker spots of moisture seen in the boundary layer in panels (d) or (f) are unlikely to be realistic since the water vapor mixing ratio should not increase with height in the boundary layer. The drier area around 1700 m between 08:00 and 09:30 UTC in panel (d) is also unrealistic. The moistening of the upper layers, dominating between 04:55 and 10:40 UTC, is determined by the boundary conditions at the top, which are forced by the linear interpolation. This is a constraint that cannot be easily assessed. Finally, if we pay attention to the curvature of the profiles in the boundary layer in panel (c), we notice that the profiles can be sorted in two categories of symmetric curvature, which has been constrained by the sign of the humidity gradient of each of the border profiles, i.e. RS1 and RS2.

So, even if the atmospheric conditions encountered during BLLAST are among the most propitious to apply the proposed method, we found difficulties which end up with reducing the skill of the method to produce good results.

## 6 Conclusions

We demonstrated in the first four sections of this paper that, although WPRs, with their first three moments, measure essential parameters for the determination of the vertical gradient of water vapor mixing ratio, the radar data cannot be used to retrieve the vertical profiles of water vapor mixing ratio independently from other sensors' data. To obtain the profiles, we applied a method already used by Tsuda et al. (2001) and other authors, which consists in using a combined retrieval algorithm exploiting the WPR measurements and RS observations at a coarser frequency. This algorithm requires an integration of the WPR and RS data along $z$, which may lead to an amplification of the errors. We improved the algorithm by using a key parameter from the radar, which is the level of the reflectivity peak value, Hlim, allowing to split the calculations in two parts, with two different calibration coefficients accounting for two areas of different turbulence characteristics. The introduction of this level also mitigated the errors by replacing a long integration by two shorter ones. As Hlim usually corresponded to a strong moisture inversion, there was no problem to connect the results of the two integrations at the level of the discontinuity.

After assessing the algorithm at the time of the RS observations, we applied it between two RS profiles, to obtain humidity profiles at a finer time resolution and to check the performance of the combined algorithm with respect to a simple RS time interpolation. We used, when available, simultaneous lidar data to assess the results. The set of data that enabled this comparison was collected during a period seldom characterized by the presence of clear-sky conditions, while cloudy conditions were prevailing (HYMEX SOP1). In the presence of clouds, the lidar beam is rapidly attenuated above cloud base, so that the assessment could only be made in the lower portion of the profiles.

We obtained some satisfactory results, but we met some hindrances that make the method hard to apply in an entirely automatic way. These difficulties are summarized below :

- The most restrictive issue is the one associated with the top border conditions. If these are not well defined (for instance at a moisture inversion level), the error may propagate and become large at the Hlim level. The resulting profiles can also very easily move apart, towards the two constraining borders: either towards 0 g kg$^{-1}$ as the minimum value, or towards the saturated moisture content as the maximum value. For this reason, we paid special attention to the definition of the border conditions from the initial and final radiosounding, which was needed to define the border conditions for the intermediate profiles. We must recognize that we had to rectify 'by-hand' few border conditions automatically detected by the algorithm. Indeed, the approach of using a time interpolation between the initial and final radiosounding border conditions is also questionable. This is ineffective when the border radiosoundings are equally spaced from a moisture maximum for instance, which is likely to happen when the RS are spaced 12h apart. However, this frequency for RSs is typically considered in most Met Offices all over the world. In some cases, this difficulty could be overcome by using a ground station to document the bottom conditions, provided that the layer between the surface and the first radar gate is well mixed. This happened hardly ever during HYMEX SOP1, since many profiles were measured under stratified conditions. The other dataset that was collected under summer nice weather conditions could have provided this opportunity, at least during the periods when the mixed layer was well developed. Anyhow, the top border conditions could not be documented similarly. Even if the moisture content is weaker at higher levels, it could vary between 1 g kg$^{-1}$ and 5-6 g kg$^{-1}$, since the vertical range of the radar was seldom larger than 3 km.

- Our algorithm, relying on the determination of the Hlim level, was not successful when more than one strong moisture inversion occurred. It was often the case for the BLLAST dataset, since another strong inversion (associated with a secondary $Cn^2$ peak value) was often found at the top of the RS border profiles. Usually moisture drastically decreases at this level and air becomes too dry to allow any upper level detection by the radar. For these cases, we cut the top of the profiles, to avoid a wrong estimation of the top border conditions and a wrong estimation of Hlim.

- Although pressure and temperature are secondary parameters in the algorithm, so that they do not require as much accuracy as the border conditions, the profiles for these parameters have to be provided. These two parameters are also used to constrain the computed water vapor mixing ratio values to the saturation water vapor mixing ratio. We used a linear interpolation of the two border RS to get the intermediate $P$ and $T$ profiles. Alternatively, these profiles could be provided by model outputs, which are usually more reliable for pressure and temperature than they are for humidity.

- The constraint on the sign of the humidity gradient is also an issue that can hardly be solved by a simple interpolation or a continuity constraint in time. Some authors constraint their results by the integrated water content measured with a GPS. Unfortunately, this method failed with our datasets, since the amount of humidity accumulated in the atmospheric layer explored by the radar, with respect to the humidity amount of the whole column observed by GPS, was varying with the time. This was probably due to the limited coverage range of the UHF profiler, and could perhaps have been avoided by using a combination of UHF and VHF measurements. Unfortunately, such a combination was not available.

- We must highlight the fact that the moist HYMEX conditions probably correspond to the most challenging conditions, even if those are frequently encountered at mid-latitudes. During HYMEX SOP1, the air was very often close to saturation so that the radar targets could be clear air or a mixing of clear air and rainfall droplets, with successive layers of different properties of the WPR backscattering. Anyhow, the method we proposed to calibrate the radar measurements, based on the use of varying $\alpha^2$ coefficients for each situation and for two different layers in the troposphere, corresponding to varying properties of either turbulence or the scattering properties of the air, revealed to be essential. Nevertheless, the variations in the atmospheric turbulence state was a dominant element, as in fact the BLLAST dataset, that included a variety of turbulence states, provided the largest scattering in the $\alpha^2$ coefficients.

Finally, we demonstrated that the combined RS-radar algorithm used to retrieve the humidity profiles outperforms a simple interpolation of the RS observations. The radar is especially skilled at determining the evolution of the transition layers, which is usually an issue when using other remote-sensing measurements such as, for example, radiometer measurements. However, the present method should be used with caution, and is probably more adequate in postprocessing a dataset for scientific purpose than for a blind use in an automatic platform.

*Acknowledgements.* Data were obtained from the HyMeX program, sponsored by grants from MISTRALS/HyMeX and ANR-11-BS56-0005 IODA-MED through the Fonds Européen de Développement Régional of the European Operational Program 2007-2013. BLLAST field experiment was made possible thanks to the contribution of several institutions and supports : INSU-CNRS (Institut National des Sciences de l'Univers, Centre national de la Recherche Scientifique, LEFE-IDAO program), Météo-France, Observatoire Midi-Pyrénées (University of Toulouse), EUFAR (EUropean Facility for Airborne Research) and COST ES0802 (European Cooperation in the field of Scientific and Technical). BLLAST field experiment was hosted by the instrumented site of Centre de Recherches Atmosphériques, Lannemezan, France (Observatoire Midi-Pyrénées, Laboratoire d'Aérologie). We also thank the CNRM team (Météo-France, Toulouse) for operating the Candillargues radar and launching the radiosoundings and SEDOO (Observatoire Midi-Pyrénées, Toulouse, France) for their help in quick-look providing and data-base management for both BLLAST and HyMex experiments.

## References


Angevine, W. M., White, A. B., and Avery, S. K.: Boundary-layer depth and entrainment zone characterization with a boundary-layer profiler, Bound.-Layer Meteor., p. 375–385, 1994.

Atlas, D., Srivastava, R., and Sekhon, R.: Doppler radar characteristics of precipitation at vertical incidence, Rev. Geophys. Space Phys., pp. 1–35, 1973.

Bianco, L., Cimini, D., Marzano, F. S., and Ware, R.: Combining Microwave Radiometer and Wind Profiler Radar Measurements for High-Resolution Atmospheric Humidity Profiling, Journal of Atmospheric and Oceanic Technology, 22, 949–965, doi:10.1175/JTECH1771.1, http://journals.ametsoc.org/doi/abs/10.1175/JTECH1771.1, 2005.

Campistron, B. and Réchou, A.: Rain kinetic energy measurement with a UHF wind profiler, 13th workshop on Technical and Scientific Aspects of MST Radar (MST13), Kühlungsborn, 19-23 March, Germany, 2012.

Campistron, B., Saïd, F., Delbarre, H., Augustin, P., and Lambert, D.: Rain Profiling with a UHF Wind Profiler and its Application to Soil Erosion Study., HyMeX 7th international conference, Cassis, France, 2013.

Chu, Y.-H. and Su, C.-L.: An Investigation of the Slope–Shape Relation for Gamma Raindrop Size Distribution, Journal of Applied Meteorology and Climatology, 47, 2531–2544, doi:10.1175/2008JAMC1755.1, http://journals.ametsoc.org/doi/abs/10.1175/2008JAMC1755.1, 2008.

Di Girolamo, P.: Rotational Raman Lidar measurements of atmospheric temperature in the UV, Geophysical Research Letters, 31, doi:10.1029/2003GL018342, http://doi.wiley.com/10.1029/2003GL018342, 2004.

Di Girolamo, P., Summa, D., and Ferretti, R.: Multiparameter Raman Lidar Measurements for the Characterization of a Dry Stratospheric Intrusion Event, Journal of Atmospheric and Oceanic Technology, 26, 1742–1762, doi:10.1175/2009JTECHA1253.1, http://journals.ametsoc.org/doi/abs/10.1175/2009JTECHA1253.1, 2009.

Di Girolamo, P., Flamant, C., Cacciani, M., Richard, E., Ducrocq, V., Summa, D., Stelitano, D., Fourrié, N., and Saïd, F.: Observation of low-level wind reversals in the Gulf of Lion area and their impact on the water vapour variability: Low-Level Wind Reversals and their Impact on Water Vapour Variability, Quarterly Journal of the Royal Meteorological Society, 142, 153–172, doi:10.1002/qj.2767, http://doi.wiley.com/10.1002/qj.2767, 2016.

Doviak, R. J. and Zrnic, D. S.: Doppler Radar and Weather Observations, Elsevier science, Oxford, 1984.

Ducrocq, V., Braud, I., Davolio, S., Ferretti, R., Flamant, C., Jansa, A., Kalthoff, N., Richard, E., Taupier-Letage, I., Ayral, P.-A., Belamari, S., Berne, A., Borga, M., Boudevillain, B., Bock, O., Boichard, J.-L., Bouin, M.-N., Bousquet, O., Bouvier, C., Chiggiato, J., Cimini, D., Corsmeier, U., Coppola, L., Cocquerez, P., Defer, E., Delanoe, J., Di Girolamo, P., Doerenbecher, A., Drobinski, P., Dufournet, Y., Fourrie, N., Gourley, J. J., Labatut, L., Lambert, D., Le Coz, J., Marzano, F. S., Molinie, G., Montani, A., Nord, G., Nuret, M., Ramage, K., Rison, W., Roussot, O., Saïd, F., Schwarzenboeck, A., Testor, P., Van Baelen, J., Vincendon, B., Aran, M., and Tamayo, J.: HyMeX-SOP1: The Field Campaign Dedicated to Heavy Precipitation and Flash Flooding in the Northwestern Mediterranean, Bulletin of the American Meteorological Society, 95, 1083–1100, doi:10.1175/BAMS-D-12-00244.1, 2014.

Estournel, C., Testor, P., Taupier-Letage, I., Bouin, M.-N., Coppola, L., Durand, P., Conan, P., Bosse, A., Brilouet, P.-E., Beguery, L., Belamari, S., Béranger, K., Beuvier, J., Bourras, D., Canut, G., Doerenbecher, A., Durrieu de Madron, X., D'Ortenzio, F., Drobinski, P., Ducrocq, V., Fourrié, N., Giordani, H., Houpert, L., Labatut, L., Lebeaupin Brossier, C., Nuret, M., Prieur, L., Roussot, O., Seyfried, L., and Somot, S.: HyMeX-SOP2: The Field Campaign Dedicated to Dense Water Formation in the Northwestern Mediterranean, Oceanography, 29, 196–206, 2016.

Foote, G. B. and Du Toit, P. S.: Terminal Velocity of Raindrops Aloft, Journal of Applied Meteorology, 8, 249–253, doi:10.1175/1520-0450(1969)008<0249:TVORA>2.0.CO;2, http://journals.ametsoc.org/doi/abs/10.1175/1520-0450%281969%29008%3C0249%3ATVORA%3E2.0.CO%3B2, 1969.

Furumoto, J., Kurimoto, K., and Tsuda, T.: Continuous Observations of Humidity Profiles with the MU Radar–RASS Combined with GPS and Radiosonde Measurements, Journal of Atmospheric and Oceanic Technology, 20, 23–41, doi:10.1175/1520-0426(2003)020<0023:COOHPW>2.0.CO;2, http://journals.ametsoc.org/doi/abs/10.1175/1520-0426%282003%29020%3C0023%3ACOOHPW%3E2.0.CO%3B2, 2003.

Furumoto, J.-I., Tsuda, T., Iwai, S., and Kozu, T.: Continuous Humidity Monitoring in a Tropical Region with the Equatorial Atmosphere Radar, Journal of Atmospheric and Oceanic Technology, 23, 538–551, doi:10.1175/JTECH1868.1, http://journals.ametsoc.org/doi/abs/10.1175/JTECH1868.1, 2006.

Furumoto, J.-I., Imura, S., Tsuda, T., Seko, H., Tsuyuki, T., and Saito, K.: The Variational Assimilation Method for the Retrieval of Humidity Profiles with the Wind-Profiling Radar, Journal of Atmospheric and Oceanic Technology, 24, 1525–1545, doi:10.1175/JTECH2074.1, http://journals.ametsoc.org/doi/abs/10.1175/JTECH2074.1, 2007.

Gossard, E. E. and Sengupta, N.: Measuring gradients of meteorological properties in elevated layers with a surface-based Doppler radar, Radio Sci., p. 625–639, 1988.

Gossard, E. E., Chadwick, R. B., Neff, W. D., and Moran, K. P.: The Use of Ground-Based Doppler Radars to Measure Gradients, Fluxes and Structure Parameters in Elevated Layers, Journal of Applied Meteorology, 21, 211–226, doi:10.1175/1520-0450(1982)021<0211:TUOGBD>2.0.CO;2, http://journals.ametsoc.org/doi/abs/10.1175/1520-0450%281982%29021%3C0211%3ATUOGBD%3E2.0.CO%3B2, 1982.

Gossard, E. E., Wolfe, D. E., Moran, K. P., Paulus, R. A., Anderson, K. D., and Rogers, L. T.: Measurement of Clear-Air Gradients and Turbulence Properties with Radar Wind Profilers, Journal of Atmospheric and Oceanic Technology, 15, 321–342, doi:10.1175/1520-0426(1998)015<0321:MOCAGA>2.0.CO;2, http://journals.ametsoc.org/doi/abs/10.1175/1520-0426%281998%29015%3C0321%3AMOCAGA%3E2.0.CO%3B2, 1998.

Gossard, E. E., Gutman, S., Stankov, B. B., and Wolfe, D. E.: Profiles of radiorefractive index and humidity derived from radar wind profilers and the Global Positioning System, Radio Sci., pp. 371–383, 1999.

Heo, Jacoby-Koaly, S., Kim, K., Campistron, B., Benech, B., and .Jung, E.: Use of the doppler spectral width to improve the estimation of the convective boundary layer height from UHF wind profiler observations, Atmospherique Ocean Technologie, pp. 408 – 424, 2003.

Hocking, W. K.: Two years of continuous measurements of turbulence parameters in the upper mesosphere and lower thermosphere made with a 2-MHz radar, Journal of Geophysical Research, 93, 2475, doi:10.1029/JD093iD03p02475, http://doi.wiley.com/10.1029/JD093iD03p02475, 1988.

Imura, S., Furumoto, J.-I., Tsuda, T., and Nakamura, T.: Estimation of Humidity Profiles by Combining Co-Located VHF and UHF Wind-Profiling Radar Observation, Journal of the Meteorological Society of Japan. Ser. II, 85, 301–319, doi:10.2151/jmsj.85.301, 2007.

Jacoby-Koaly, S., Campistron, B., Bernard, S., Bénech, B., Ardhuin-Girard, F., Dessens, J., Dupont, E., and Carissimo, B.: Turbulent Dissipation Rate in the Boundary Layer via UHF Wind Profiler Doppler Spectral Width Measurements, Boundary-Layer Meteor., pp. 361–389, 2002.

Klaus, V., Bianco, L., Gaffard, C., Matabuena, M., and Hewison, T. J.: Combining UHF radar wind profiler and microwave radiometer for the estimation of atmospheric humidity profiles, Meteorologische Zeitschrift, 15, 87–97, doi:10.1127/0941-2948/2006/0102, 2006.

Lothon, M., Lohou, F., Pino, D., Couvreux, F., Pardyjak, E. R., Reuder, J., Vilà-Guerau de Arellano, J., Durand, P., Hartogensis, O., Legain, D., Augustin, P., Gioli, B., Lenschow, D. H., Faloona, I., Yagüe, C., Alexander, D. C., Angevine, W. M., Bargain, E., Barrié, J., Bazile, E., Bezombes, Y., Blay-Carreras, E., van de Boer, A., Boichard, J. L., Bourdon, A., Butet, A., Campistron, B., de Coster, O., Cuxart, J., Dabas, A., Darbieu, C., Deboudt, K., Delbarre, H., Derrien, S., Flament, P., Fourmentin, M., Garai, A., Gibert, F., Graf, A., Groebner, J., Guichard, F., Jiménez, M. A., Jonassen, M., van den Kroonenberg, A., Magliulo, V., Martin, S., Martinez, D., Mastrorillo, L., Moene, A. F., Molinos, F., Moulin, E., Pietersen, H. P., Piguet, B., Pique, E., Román-Cascón, C., Rufin-Soler, C., Saïd, F., Sastre-Marugán, M., Seity, Y., Steeneveld, G. J., Toscano, P., Traullé, O., Tzanos, D., Wacker, S., Wildmann, N., and Zaldei, A.: The BLLAST field experiment: Boundary-Layer Late Afternoon and Sunset Turbulence, Atmospheric Chemistry and Physics, 14, 10 931–10 960, doi:10.5194/acp-14-10931-2014, http://www.atmos-chem-phys.net/14/10931/2014/, 2014.

Miloshevich, L. M., Vömel, H., Whiteman, D. N., Lesht, B. M., Schmidlin, F. J., and Russo, F.: Absolute accuracy of water vapor measurements from six operational radiosonde types launched during AWEX-G and implications for AIRS validation, Journal of Geophysical Research, 111, doi:10.1029/2005JD006083, http://doi.wiley.com/10.1029/2005JD006083, 2006.

Nash, J., Oakley, T., Vömel, H., and Wei, L.: WMO Intercomparison of High Quality Radiosonde Systems, Tech. Rep. IOM 107 (TD 1580), WMO Library, Yangjiang, China, 2011.

Ottersten, H.: Radar backscattering from the turbulent clear atmosphere, Radio Science, 4, 1251–1255, 1969.

Saïd, F., Campistron, B., Delbarre, H., Canut, G., Doerenbecher, A., Durand, P., Fourrié, N., Lambert, D., and Legain, D.: Offshore winds obtained from a network of wind-profiler radars during HyMeX: 3D Wind Fields during HyMeX, Quarterly Journal of the Royal Meteorological Society, 142, 23–42, doi:10.1002/qj.2749, http://doi.wiley.com/10.1002/qj.2749, 2016.

Stankov, B. B., Westwater, E. R., and Gossard, E. E.: Use of Wind Profiler Estimates of Significant Moisture Gradients to Improve Humidity Profile Retrieval, Journal of Atmospheric and Oceanic Technology, 13, 1285–1290, doi:10.1175/1520-0426(1996)013<1285:UOWPEO>2.0.CO;2, http://journals.ametsoc.org/doi/abs/10.1175/1520-0426%281996%29013%3C1285%3AUOWPEO%3E2.0.CO%3B2, 1996.

Stankov, B. B., Gossard, E. E., Weber, B. L., Lataitis, R. J., White, A. B., Wolfe, D. E., Welsh, D. C., and Strauch, R. G.: Humidity Gradient Profiles from Wind Profiling Radars Using the NOAA/ETL Advanced Signal Processing System (SPS), Journal of Atmospheric and Oceanic Technology, 20, 3–22, doi:10.1175/1520-0426(2003)020<0003:HGPFWP>2.0.CO;2, http://journals.ametsoc.org/doi/abs/10.1175/1520-0426%282003%29020%3C0003%3AHGPFWP%3E2.0.CO%3B2, 2003.

Tatarskii, V. I., ed.: Wave propagation in turbulent medium, McGraw-Hill,New-York, New-York, translated by r. a. silverman edn., 1971.

Tsuda, T., Miyamoto, M., and Furumoto, J.-i.: Estimation of a Humidity Profile Using Turbulence Echo Characteristics, Journal of Atmospheric and Oceanic Technology, 18, 1214–1222, doi:10.1175/1520-0426(2001)018<1214:EOAHPU>2.0.CO;2, http://journals.ametsoc.org/doi/abs/10.1175/1520-0426%282001%29018%3C1214%3AEOAHPU%3E2.0.CO%3B2, 2001.

Ulrich, C.: Natural variations in the analytic form of the raindrop size distribution, J. Climate Appl. Meteor., pp. 1764–1775, 1983.

VanZandt, T. E., Green, J. L., Gage, K. S., and Clark, W. L.: Vertical profiles of refractivity turbulence structure constant: Comparison of observations by the Sunset Radar with a new theoretical model, Radio Science, 13, 819–829, doi:10.1029/RS013i005p00819, http://doi.wiley.com/10.1029/RS013i005p00819, 1978.

White, A. B., Lataitis, R. J., and Lawrence, R. S.: Space and Time Filtering of Remotely Sensed Velocity Turbulence, Journal of Atmospheric and Oceanic Technology, 16, 1967–1972, doi:10.1175/1520-0426(1999)016<1967:SATFOR>2.0.CO;2, http://journals.ametsoc.org/doi/abs/10.1175/1520-0426%281999%29016%3C1967%3ASATFOR%3E2.0.CO%3B2, 1999.

Atmos. Meas. Tech. Discuss., https://doi.org/10.5194/amt-2017-265
Manuscript under review for journal Atmos. Meas. Tech.
Discussion started: 8 September 2017


Atmospheric Measurement Techniques Discussions
Open Access

**Table 1.** *Correlation coefficient $R^2$ of the linear regression between radar and RS humidity values for the three data sets. Mean bias (RS minus radar) and standard deviation for the whole dataset is also specified, together with the largest standard deviation value in the dataset. 'lm' and 'hm' stand for low mode and high mode, respectively. The results for BLLAST are calculated in the reduced range 845-4000 m and 895-4400 m ASL for the low mode and high mode, respectively.*

| dataset | mode | $R^2$ coef. | mean bias (g kg$^{-1}$) | mean std (g kg$^{-1}$) | max std (g kg$^{-1}$) |
|---|---|---|---|---|---|
| BLLAST | lm | 0.87 | -0.07 | 0.82 | 1.49 |
| | hm | 0.73 | 0.36 | 1.19 | 1.58 |
| HyMeX | lm | 0.89 | 0.19 | 0.92 | 2.25 |
| September | hm | 0.92 | 0.02 | 0.70 | 1.69 |
| HyMeX | lm | 0.85 | 0.24 | 0.85 | 1.24 |
| October | hm | 0.87 | 0.08 | 0.98 | 1.20 |
| HyMeX | lm | 0.94 | 0.04 | 0.17 | 0.3 |
| February | hm | 0.93 | 0.01 | 0.18 | 0.32 |

**Table 2.** *Parameters used to retrieve 15 min-spaced vertical profiles of q in the time interval between two radiosoundings RS1 and RS2. Hlim serves to apply the convenient calibration coefficient and to merge the two integrals.*

| | |
|---|---|
| **Parameters used to calculate $M^2(z)$ in Eq. (15)** | |
| $C_n^2(t,z)$, $\epsilon(t,z)$, $\frac{dV(t,z)}{dz}$ : | provided by the radar every 15 min |
| $\alpha^2(t)$ lower layers : | from a 15 min-interpolation between the radar/RS1 and radar/RS2 calibration coefficients |
| $\alpha^2(t)$ upper layers : | from a 15 min-interpolation between the radar/RS1 and radar/RS2 calibration coefficients |
| **Parameters used to retrieve $q(z)$ from Eq. (12)** | |
| $\theta(t,z)$, $P(t,z)$ : | 15 min-interpolated profiles from RS1 and RS2 $\theta(z)$, and $P(z)$ |
| $q_o(t)$ bottom : | 15 min-interpolated $q$ from RS1 and RS2 at the lower common level |
| $q_o(t)$ top : | 15 min-interpolated $q$ from RS1 and RS2 at the upper common level |
| $Hlim(t)$ : | extracted from the radar $C_n^2$ profile every 15 min (usually the peak value) |
| constraint of sign of $M$ at level $z$ and time $t$: | depends on the sign of $M(z,t)$ (or humidity vertical gradient) for RS1 and RS2 |
| $q(t,z)$ saturated value (to constraint $q(t,z)$) : | from a 15 min-interpolation of $T(z)$ and $P(z)$ between RS1 and RS2 |

Atmos. Meas. Tech. Discuss., https://doi.org/10.5194/amt-2017-265
Manuscript under review for journal Atmos. Meas. Tech.
Discussion started: 8 September 2017


Atmospheric Measurement Techniques
Discussions

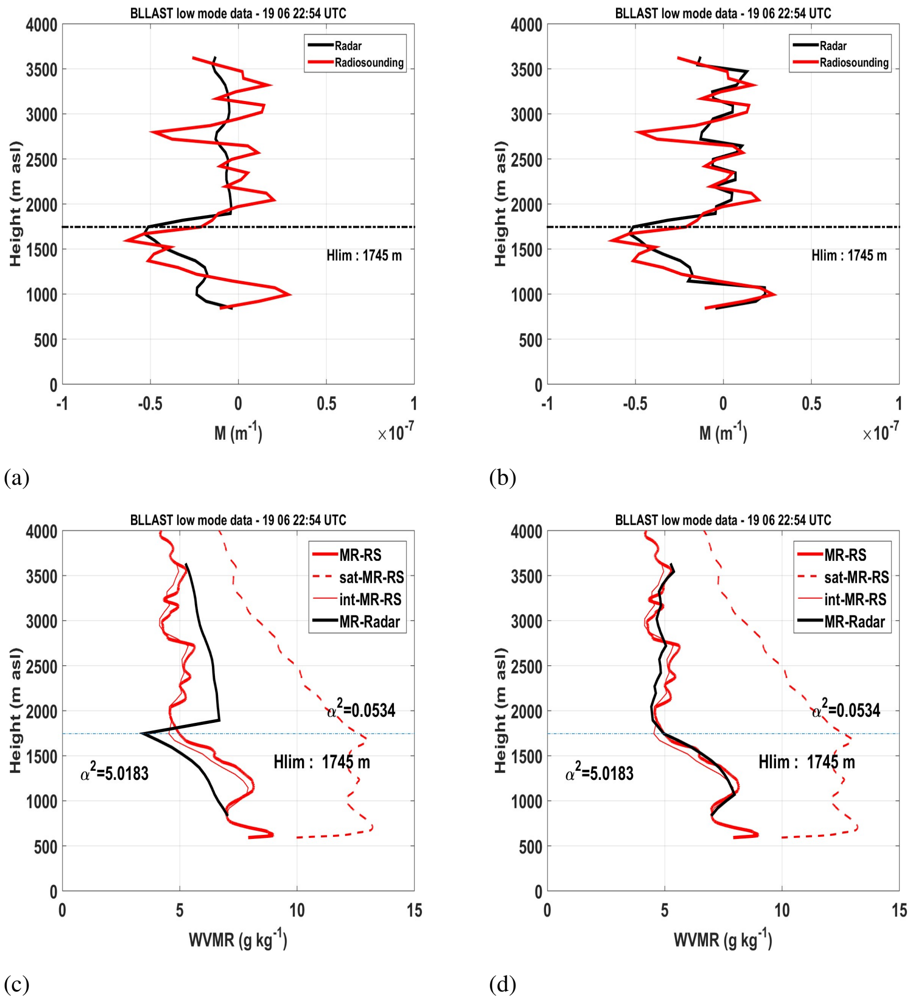


**Figure 1.** *Vertical profiles of refractivity gradient (panels (a) and (b)) and humidity (panels (c) and (d)) using a systematic negative sign for M (panels (a) and (c)), or after assigning to $M$ the sign of $M$ provided by the RS observations (panels (b) and (d)). RS values are red solid lines and radar values are black solid lines. The thin red lines identify the humidity profiles retrieved from the integration of $M_{RS}$ after averaging the RS observations by slices of 75 m, to match the vertical resolution of the radar. The red dashed line is for the saturated humidity profile. The horizontal dashed line delineates Hlim, the transition level used to separate the upper and lower part of the profile. The two values of $\alpha^2$ , over or below Hlim are also indicated.*

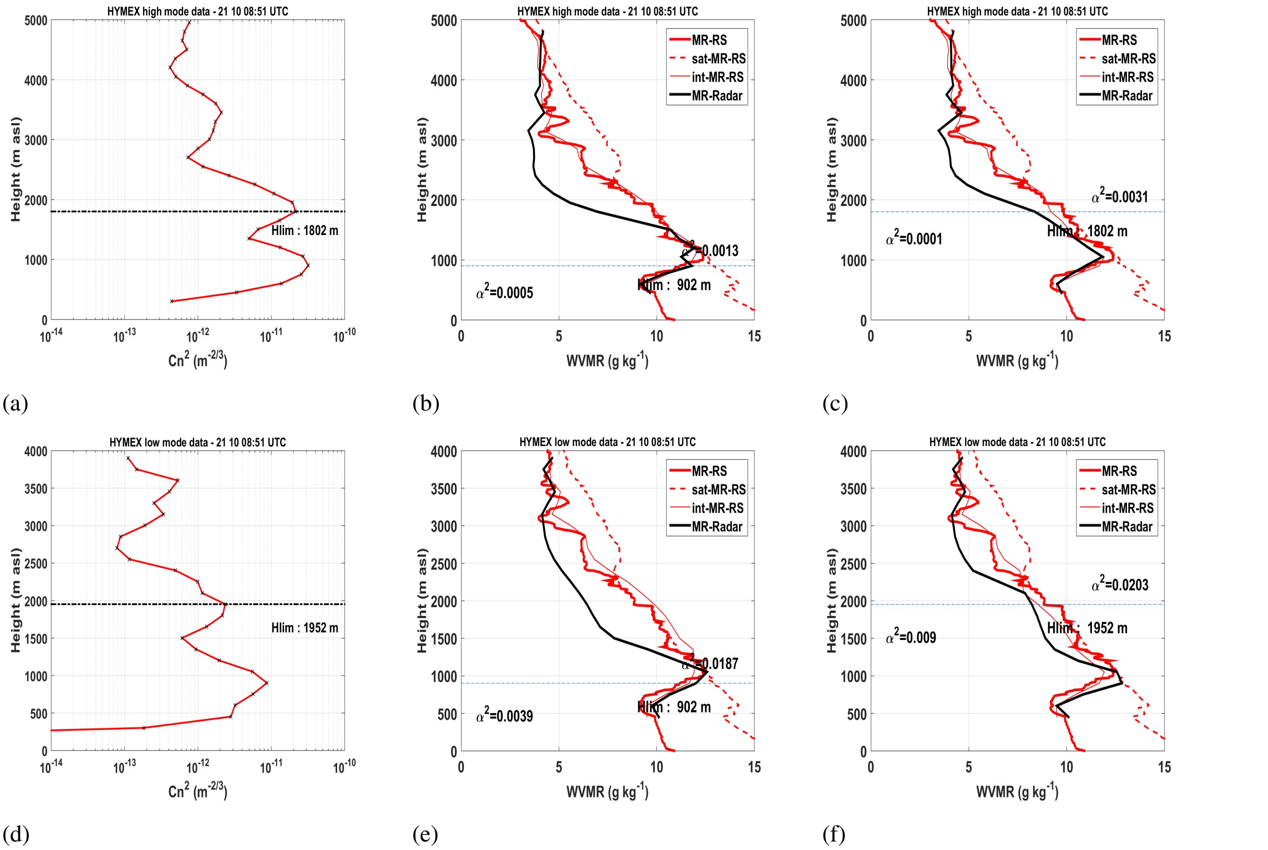


**Figure 2.** *Radar turbulence structure parameter $Cn^2$ (panels (a) and (d)) and WVMR profiles (same details as in Fig. 1 (c)) for different Hlim levels. In panels (b) and (e), Hlim corresponds to the dominant $Cn^2$ peak observed in panels (a) and (d) respectively. In panels (c) and (f), a different relative maximum of the $Cn^2$ profile is considered to identify Hlim. The first row is for the high mode (vertical resolution 375 m, interpolated every 150 m) and the second for the low mode (vertical resolution 150 m).*

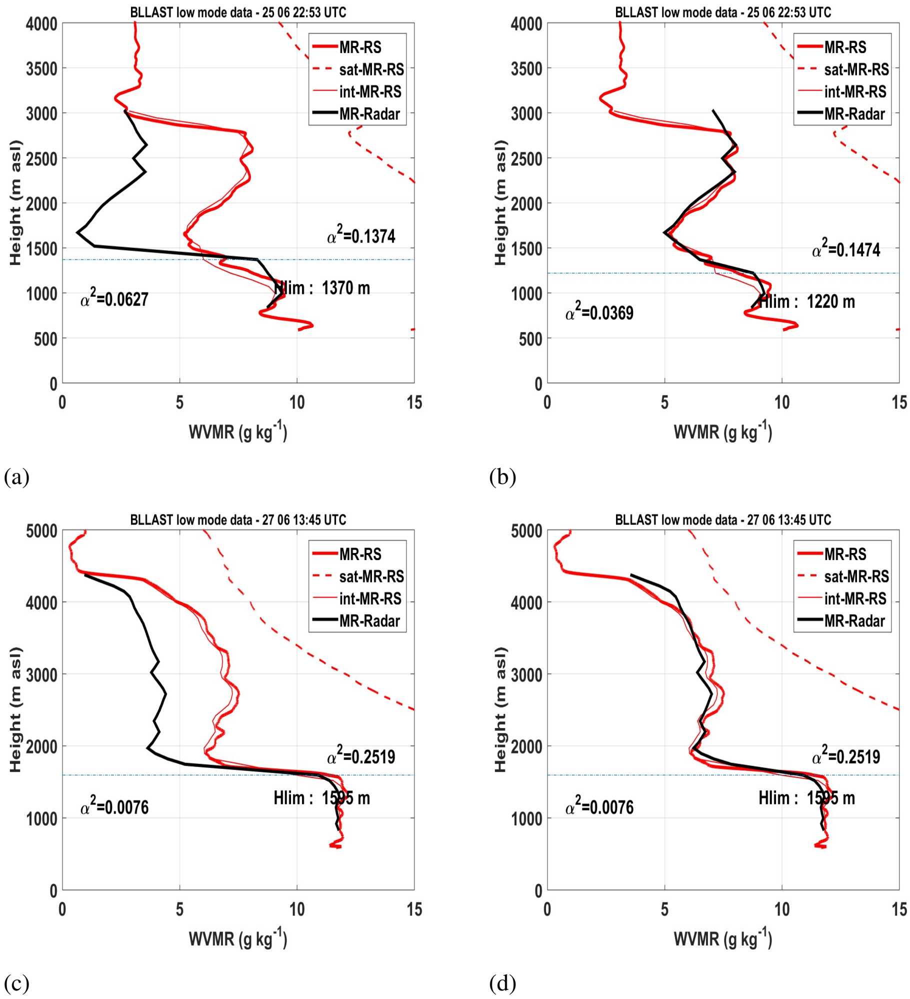


**Figure 3.** *Vertical profiles of WVMR using an automatic detection of the $q_o$ upper initial condition (panels (a) and (c)) or after the adjustment of the upper initial condition (panels (b) and (d)) for two different profiles from the BLLAST data set. The vertical resolution is 75 m. Same details as in Fig. 1 (c).*

Atmos. Meas. Tech. Discuss., https://doi.org/10.5194/amt-2017-265
Manuscript under review for journal Atmos. Meas. Tech.
Discussion started: 8 September 2017

Atmospheric Measurement Techniques
Open Access
Discussions

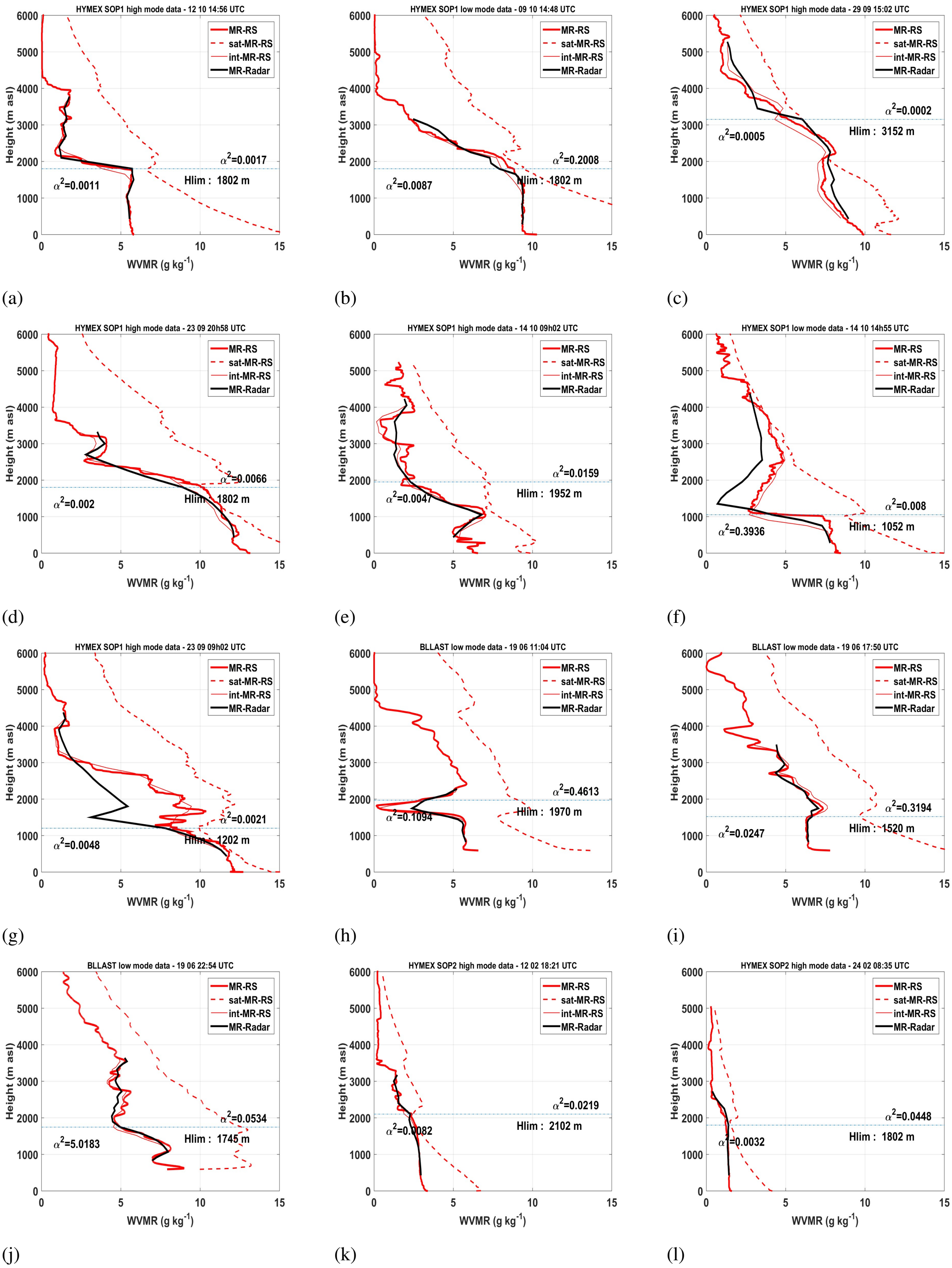


**Figure 4.** *Some selected results from HYMEX SOP1 (panels (a) to (g)), HYMEX SOP2 (panels (k),(l)) and BLLAST (panels (h) to (j)). Same details as in Fig. 1 (c).*

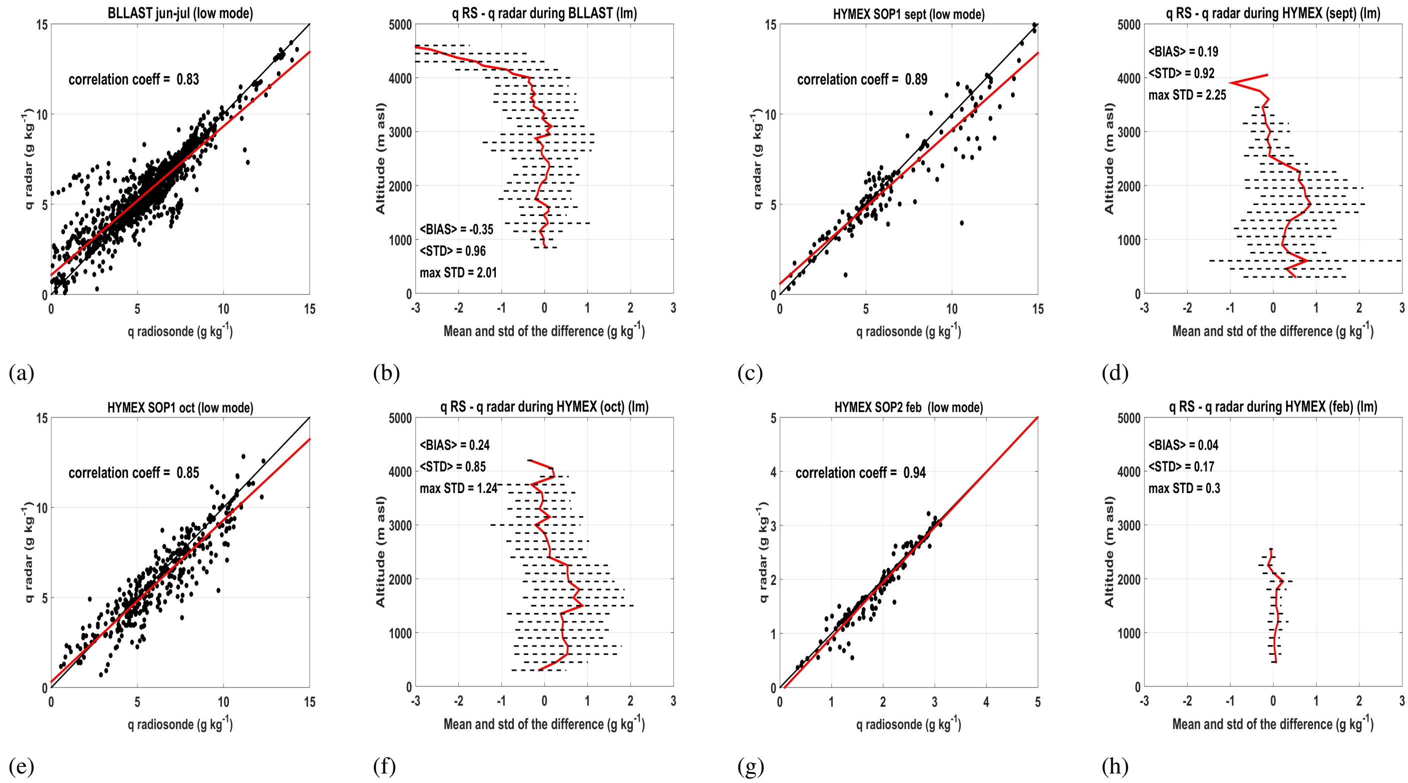


**Figure 5.** *Panels (a), (c), (e) and (g) : scatterplots of the radar versus RS WVMR during June and July 2011 (BLLAST), September 2012 (HyMeX SOP1), October 2012 (HyMeX SOP1) and February 2013 (HyMeX SOP2), respectively, with the linear regression line (in red) and the 1:1 slope line (in black). The* $R^2$ *correlation coefficient of the regression is also indicated. Panels (b), (d), (f) and (h) : vertical profiles of the difference between the RS observation and radar estimation for the same data sets* $\pm$ *the standard deviation per level. The mean bias and standard deviation for the whole dataset are shown, along with the largest standard deviation value (g* $kg^{-1}$*).*

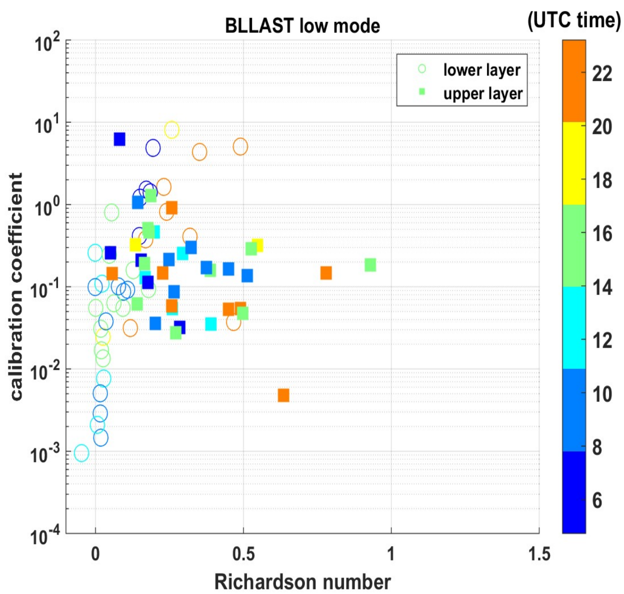


**Figure 6.** *The $\alpha^2$ calibration coefficients obtained with the BLLAST dataset in low mode as a function of the stratification estimated with the gradient Richardson number. The results are divided into the lower (circles) and upper part (squares) of the ABL and shown as a function of the time of the day (colored scale).*

Atmos. Meas. Tech. Discuss., https://doi.org/10.5194/amt-2017-265
Manuscript under review for journal Atmos. Meas. Tech.
Discussion started: 8 September 2017


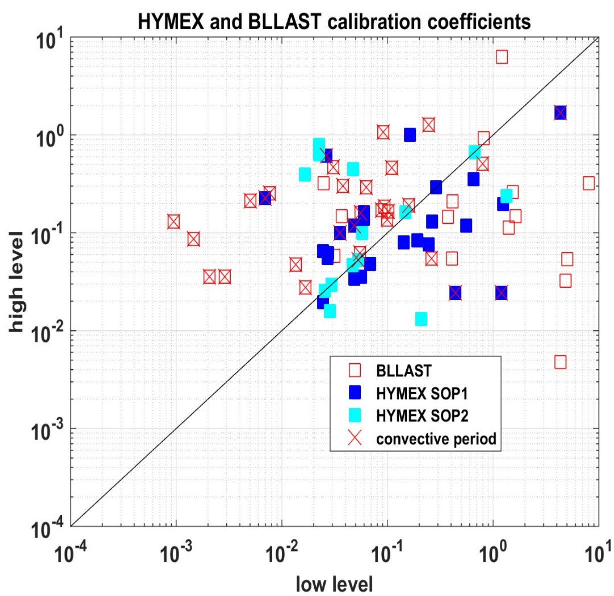


**Figure 7.** *Scatterplot of the calibration coefficients $\alpha^2$ (high level versus low level) obtained with the BLLAST and HyMeX datasets in low mode. The crosses correspond to the profiles measured during the potentially convective period i.e. 09:30-17:00 UTC.*

Atmos. Meas. Tech. Discuss., https://doi.org/10.5194/amt-2017-265
Manuscript under review for journal Atmos. Meas. Tech.
Discussion started: 8 September 2017


Atmospheric Measurement Techniques
Discussions

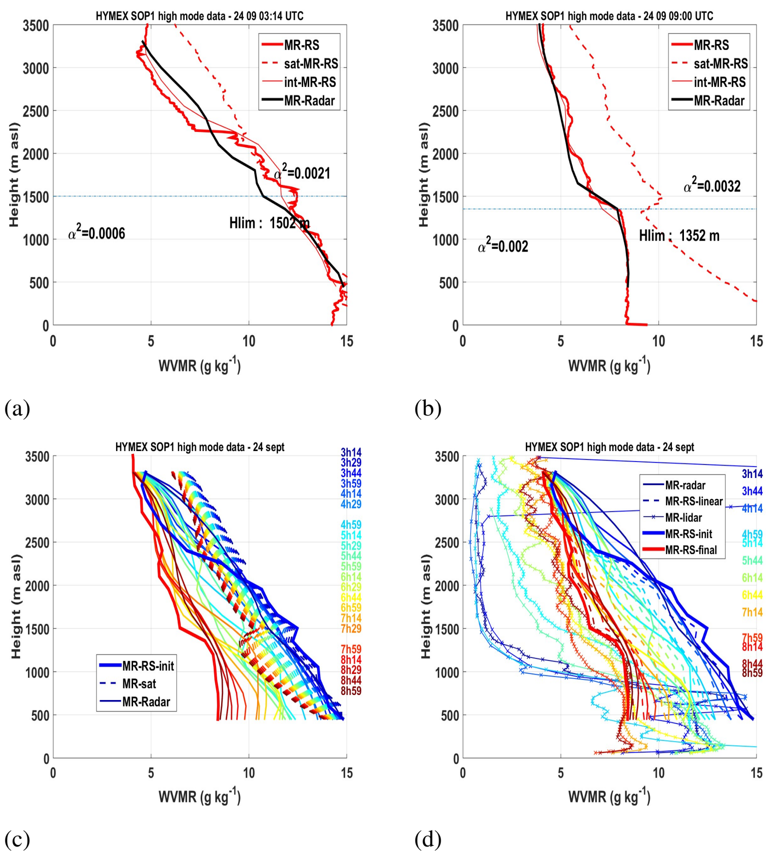


**Figure 8.** *Vertical profiles of WVMR measured during HYMEX on 24 September 2012: the radar and RS profiles used as time border conditions are shown in panels (a) and (b) with the same details as in Fig. 4. These border conditions are reproduced in panels (c) and (d) with the thick blue solid lines for RS1 (03:14 UTC) and red one for RS2 (09:00 UTC). Intermediate radar profiles (thin solid lines) and corresponding saturated water vapor profiles (dashed lines) are presented in panel (c). Panel (d) shows the lidar humidity profiles (thin lines with crosses), the radar ones (thin lines) and the humidity profiles resulting from a linear interpolation between RS1 and RS2 (dashed lines).*

Atmos. Meas. Tech. Discuss., https://doi.org/10.5194/amt-2017-265
Manuscript under review for journal Atmos. Meas. Tech.
Discussion started: 8 September 2017


Atmospheric Measurement Techniques
Discussions

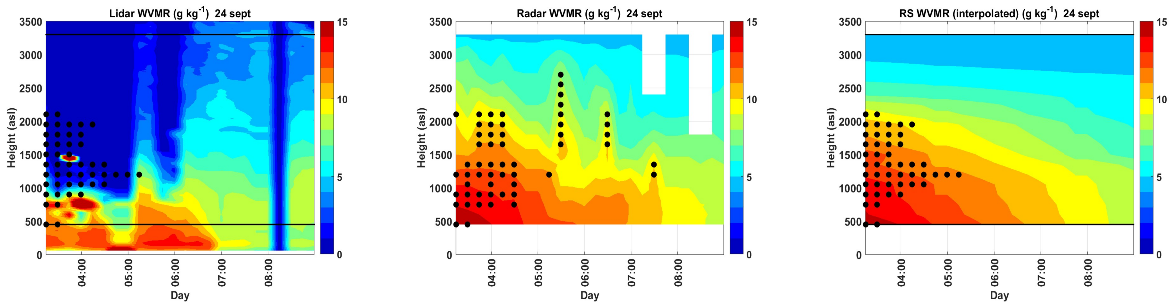


(a) (b) (c)

**Figure 9.** *Time-height cross sections of the WVMR observed on 24 September 2012 by the lidar (panel (a)), calculated from the radar data (panel (b)) and interpolated between RS1 and RS2 (panel (c)). The dots are for the radar saturated values in panel (b), and RS saturated values in panels (a) and (c).*

Atmos. Meas. Tech. Discuss., https://doi.org/10.5194/amt-2017-265
Manuscript under review for journal Atmos. Meas. Tech.
Discussion started: 8 September 2017


Atmospheric Measurement Techniques
Open Access
Discussions

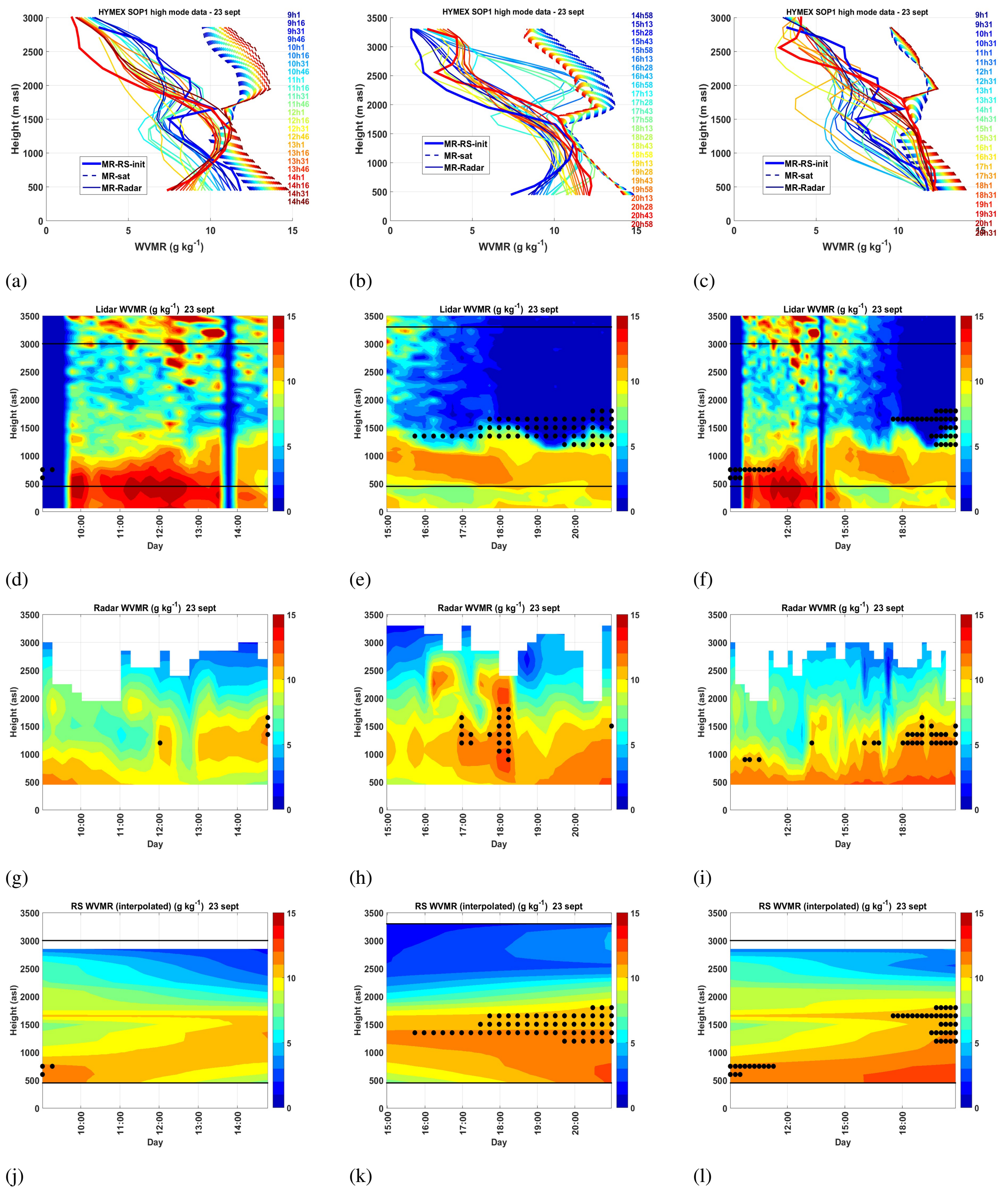


**Figure 10.** *Radar-based humidity profiles and humidity height-time cross-sections for the HYMEX 23 September case study: from RS1 (09:02 UTC, blue solid line in panel (a)) to RS2 (14:59 UTC, red solid line in panel (a)), from RS2 (blue, panel (b)) to RS3 (20:58 UTC, red solid line in panel (b)) and from RS1 (blue, panel (c)) to RS3 (red, panel (c)). First row is for the radar profiles (same details as in Fig. 8), second for the height-time mixing ratio of the lidar, third for the radar and fourth for the interpolated RS. The dots in the last three rows demarcate the saturated values as in Fig. 9.*

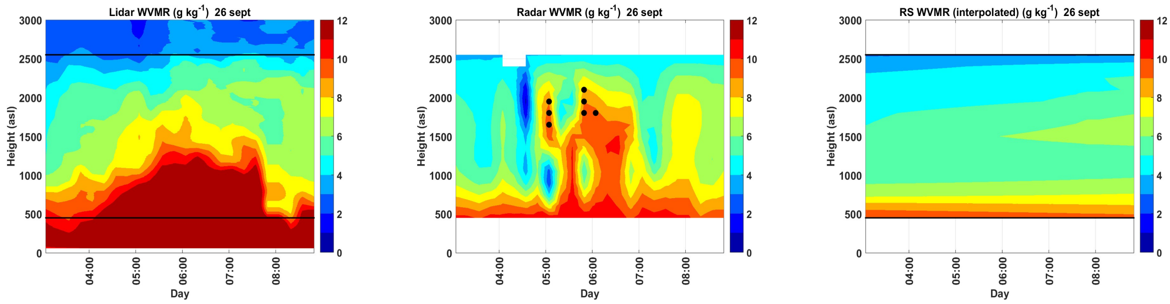


(a) (b) (c)

**Figure 11.** *Same as in Fig. 8 for 26 September 2012.*

Atmos. Meas. Tech. Discuss., https://doi.org/10.5194/amt-2017-265
Manuscript under review for journal Atmos. Meas. Tech.
Discussion started: 8 September 2017


Atmospheric Measurement Techniques
Open Access
Discussions

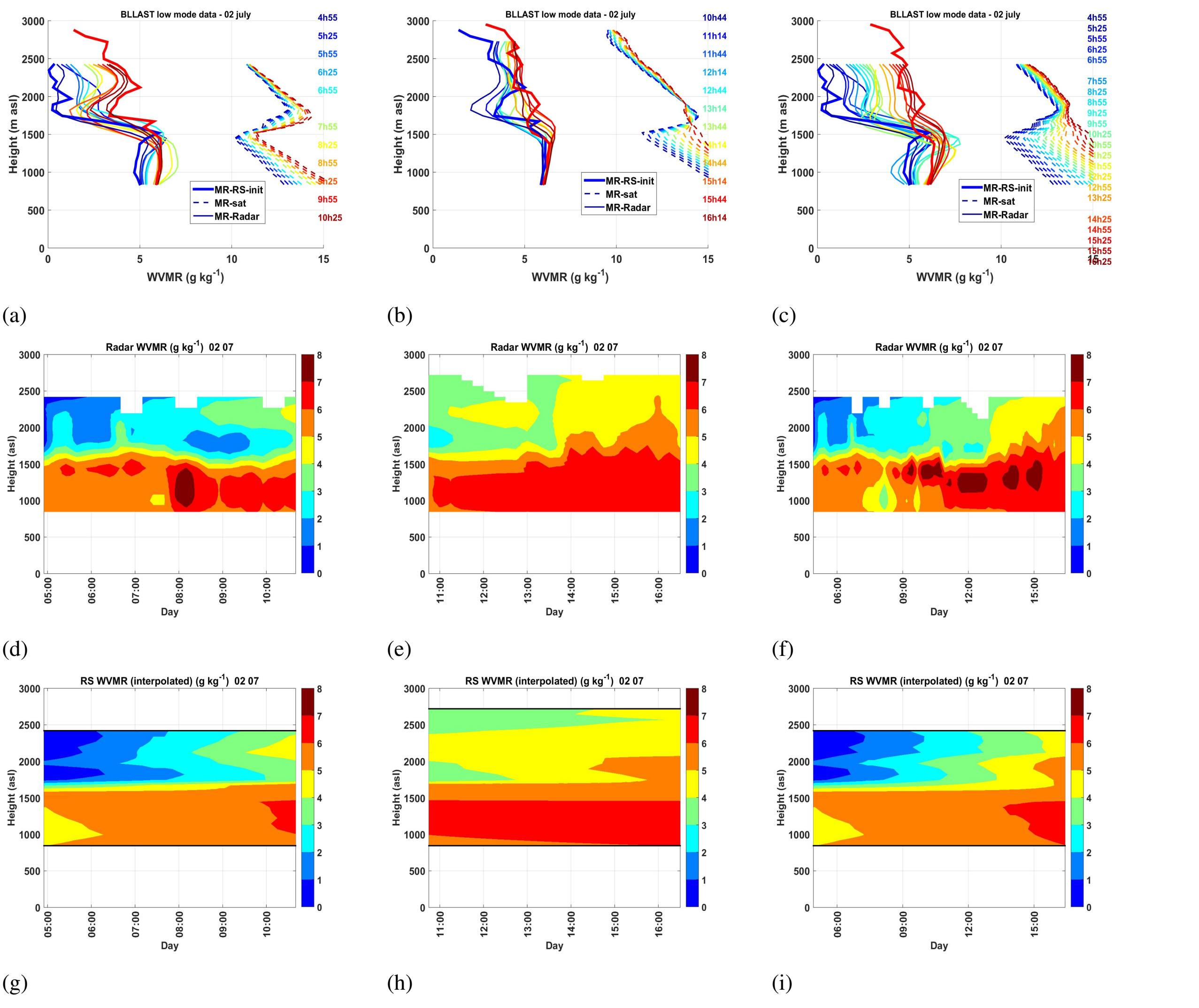


**Figure 12.** *Radar-based humidity profiles and humidity height-time cross-sections for the BLLAST 02 July 2011 case study: from RS1 (04:55 UTC, blue solid line in panel (a)) to RS2 (10:45 UTC, red solid line in panel (a)), from RS2 (blue, panel (b)) to RS3 (16:39 UTC, red solid line in panel (b)) and from RS1 (blue, panel (c)) to RS3 (red, panel (c)). First row is for the radar profiles (same details as in Fig. 8), second for the height-time mixing ratio of the radar and third for the interpolated RS.*